

## RESEARCH ARTICLE

10.1002/2017JD027371

## Special Section:

Atmospheric Gravity Wave Science in the Polar Regions and First Results from ANGWIN

## Key Points:

- Mountain waves can propagate upward to the mesosphere also under strong low-level tropospheric forcing conditions
- Required elements for propagation under strong forcing: linear propagation across tropopause, valve layer, and amplification in polar night jet
- Observations covering the atmosphere from troposphere to mesosphere were valuable to study deep propagation under strong forcing conditions

## Correspondence to:

M. Bramberger,  
martina.bramberger@dlr.de

## Citation:

Bramberger, M., Dörnbrack, A., Bossert, K., Ehard, B., Kaifler, B., Mallaun, C., ... Witschas, B. (2017). Does Strong tropospheric forcing cause large-amplitude mesospheric gravity waves? A DEEPWAVE case study. *Journal of Geophysical Research: Atmospheres*, 122, 11,422–11,443. <https://doi.org/10.1002/2017JD027371>

Received 27 JUN 2017












Accepted 4 OCT 2017

Accepted article online 8 OCT 2017

Published online 4 NOV 2017

©2017 American Geophysical Union and Crown copyright. This article is published with the permission of the Controller of HMSO and the Queen's Printer for Scotland.

## Does Strong Tropospheric Forcing Cause Large-Amplitude Mesospheric Gravity Waves? A DEEPWAVE Case Study

Martina Bramberger<sup>1</sup> , Andreas Dörnbrack<sup>1</sup> , Katrina Bossert<sup>2</sup> , Benedikt Ehard<sup>1</sup> , David C. Fritts<sup>2</sup> , Bernd Kaifler<sup>1</sup> , Christian Mallaun<sup>3</sup>, Andrew Orr<sup>4</sup> , P-Dominique Pautet<sup>5</sup> , Markus Rapp<sup>1,6</sup> , Michael J. Taylor<sup>5</sup>, Simon Vosper<sup>7</sup> , Bifford P. Williams<sup>2</sup> , and Benjamin Witschas<sup>1</sup>
<sup>1</sup>Deutsches Zentrum für Luft- und Raumfahrt, Institut für Physik der Atmosphäre, Oberpfaffenhofen, Germany, <sup>2</sup>GATS Inc., Boulder, CO, USA, <sup>3</sup>Deutsches Zentrum für Luft- und Raumfahrt, Flugexperimente, Oberpfaffenhofen, Germany, <sup>4</sup>British Antarctic Survey, Cambridge, UK, <sup>5</sup>Utah State University, Logan, UT, USA, <sup>6</sup>Meteorological Institute Munich, Ludwig-Maximilians-Universität München, Munich, Germany, <sup>7</sup>Met Office, Exeter, UK

**Abstract** On 4 July 2014, during the Deep Propagating Gravity Wave Experiment (DEEPWAVE), strong low-level horizontal winds of up to 35 m s<sup>-1</sup> over the Southern Alps, New Zealand, caused the excitation of gravity waves having the largest vertical energy fluxes of the whole campaign (38 W m<sup>-2</sup>). At the same time, large-amplitude mesospheric gravity waves were detected by the Temperature Lidar for Middle Atmospheric Research (TELMA) located at Lauder (45.0°S, 169.7°E), New Zealand. The coincidence of these two events leads to the question of whether the mesospheric gravity waves were generated by the strong tropospheric forcing. To answer this, an extensive data set is analyzed, comprising TELMA, in situ aircraft measurements, radiosondes, wind lidar measurements aboard the DLR Falcon as well as Rayleigh lidar and advanced mesospheric temperature mapper measurements aboard the National Science Foundation/National Center for Atmospheric Research Gulfstream V. These measurements are further complemented by limited area simulations using a numerical weather prediction model. This unique data set confirms that strong tropospheric forcing can cause large-amplitude gravity waves in the mesosphere, and that three essential ingredients are required to achieve this: first, nearly linear propagation across the tropopause; second, leakage through the stratospheric wind minimum; and third, amplification in the polar night jet. Stationary gravity waves were detected in all atmospheric layers up to the mesosphere with horizontal wavelengths between 20 and 100 km. The complete coverage of our data set from troposphere to mesosphere proved to be valuable to identify the processes involved in deep gravity wave propagation.

## 1. Introduction

Internal gravity waves (GWs) are ubiquitous in the atmosphere and are considered among the key processes to control global atmospheric circulation (Fritts & Alexander, 2003). By propagating horizontally and vertically over large distances, GWs transport energy and momentum and couple the atmospheric layers between the lower, middle, and upper atmosphere (Fritts & Dunkerton, 1985; Holton, 1982). Primary sources of GWs in the troposphere and lower stratosphere are wind flow over topography, shallow and deep convection, wind shears, jet streams, and geostrophic/spontaneous adjustment processes (Fritts & Alexander, 2003; Plougonven & Zhang, 2014). Higher up in the atmosphere, local flow accelerations accompanying momentum transport, wave-wave interactions, and others constitute secondary sources of GWs (e.g., Eliassen & Palm, 1961; Heale et al., 2017; Kaifler et al., 2017; Vadas et al., 2003). For topographically forced waves, linear theory predicts that the height of the obstacle, the thermal stratification, and the strength of the flow determine the magnitude of the energy and momentum transported by these waves (Gill, 1982). In this framework, strong tropospheric forcing can be associated with mountain waves accounting for large energy and momentum fluxes. Assuming favorable atmospheric background conditions and nearly linear vertical propagation, these mountain waves may propagate deeply into the middle atmosphere and cause large amplitudes in the mesosphere.

However, recent measurements during the Deep Propagating Gravity Wave Experiment (DEEPWAVE) suggest that large-amplitude mesospheric GWs observed over New Zealand (NZ) are correlated with moderate to weak low-level tropospheric forcings (Fritts et al., 2016; Kaifler, Kaifler, et al., 2015). Yet this observational finding is not surprising if one considers a nearly linear vertical propagation: weak low-level forcing across the Southern Alps usually excites small-amplitude GWs that may propagate to the middle atmosphere without becoming convectively unstable although the amplitude grows due to the decreasing density. Additionally, Smith et al. (2016) found that there is no one-to-one relationship between the magnitude of low-level forcing and the resulting energy and momentum transported by the mountain waves observed in the lower stratosphere. They rather suggest that the strength of the low-level forcing controls only the upper value of the vertical energy and momentum fluxes and it downshifts the horizontal scales of the excited GWs as the strong low-level flow becomes more terrain following than envelope following. Furthermore, recent studies using Atmospheric Infrared Sounder (AIRS) observations in the Southern Hemisphere suggest that the retrieved stratospheric wave activity at around 40 km altitude is correlated with the horizontal wind in this altitude range rather than with the low-level winds (Gisinger et al., 2017; Hoffmann et al., 2016). Thus, the propagation of mountain waves to the mesosphere is presumably primarily influenced by the ambient vertical profiles of wind and temperature.

Whenever the horizontal wind becomes zero, i.e., equal to the ground-based horizontal phase speed, mountain waves encounter a critical level (e.g., Teixeira, 2014). There, they break, dissipate, and deposit horizontal momentum (e.g., Nappo, 2013). Besides these critical levels, previous studies suggest that wind perturbations associated with GWs may induce spatially localized critical levels in the layer of minimum horizontal wind speeds ( $U$ ) in the stratosphere ( $U \lesssim 10\text{--}15\text{ m s}^{-1}$ ) (Kruse & Smith, 2015; Kruse et al., 2016; Sato, 1990). This layer, recently named as the valve layer, modifies and controls the propagation of GWs to the middle atmosphere (Kruse & Smith, 2015; Kruse et al., 2016). A connection between the stratospheric wind minimum layer and mesospheric GW activity was also observed by Kaifler, Kaifler, et al. (2015). They found that stratospheric winds  $>11\text{ m s}^{-1}$  favor the formation of strong mesospheric GW activity. Mesospheric gravity waves were observed in the majority of intensive observation periods (IOPs) during DEEPWAVE; however, only in 4 out of 16 IOPs the measurements revealed large-amplitude GWs in this altitude region (Fritts et al., 2016).

Horizontal refraction is another important process modifying GWs during their propagation. Transverse horizontal shear rotates GW phase lines, which can lead to propagation of these waves into the polar night jet (PNJ) (Dunkerton, 1984). Thus, mountain waves can be advected horizontally several thousand kilometers, which can influence the atmospheric energy and momentum budget at locations far away from the original source region of the GWs (Sato et al., 2009, 2012). Therefore, sources for mesospheric GWs are not necessarily located directly underneath the observed volume or above the GW source (e.g., Ehard et al., 2017).

In the majority of cases, previous observational studies of middle atmosphere GWs concentrated specifically on different altitude layers. For example, investigations of the evolution and propagation of GWs in the stratosphere were conducted based on, for example, aircraft measurements (e.g., Bougeault et al., 1997; Lilly & Kennedy, 1973; Smith et al., 2016; Woods & Smith, 2010) and radiosondes (e.g., Geller et al., 2013; Sato & Dunkerton, 1997). In the middle atmosphere, the evolution of GWs can be studied with all-sky imagers using the airglow of different molecules (e.g., Smith et al., 2009; Taylor et al., 2009; Wrasse et al., 2006) and lidars (e.g., Bossert et al., 2015; Kaifler, Kaifler, et al., 2015; Kaifler, Lübken, et al., 2015; Lu et al., 2015) and in situ measurements on sounding rockets (e.g., Rapp et al., 2004). These studies face the challenge that the observations are limited to specific regions that do not cover the complete vertical column from the troposphere to the middle or upper atmosphere. Therefore, the source of the observed GWs could only be inferred from derived GW characteristics such as, for example, phase speed, direction of propagation or location, and with the help of ray tracing (e.g., Ehard et al., 2017; Vadas et al., 2009). On the other hand, the airglow observations of stationary wave patterns over the Southern Andes by Smith et al. (2009) or over Auckland Islands by Pautet et al. (2016) clearly suggest topographic forcing as the only conceivable source. One of the ultimate goals of DEEPWAVE was to learn more about the propagation of mountain waves on their way to the middle atmosphere. Therefore, observations during DEEPWAVE not only used two research aircraft to broaden the geographical range but also deployed new instruments allowing observations covering the complete vertical column from the troposphere to the middle atmosphere. For a comprehensive overview of the observational strategies employed during DEEPWAVE, please refer to Fritts et al. (2016).

**Table 1**

Overview of the East-West Oriented FF04, FF05, and RF16 Legs Across the SI of New Zealand, Revealing the Altitude, Mean Time and Length of Each Leg

	Leg number	Altitude (km)	Time (UTC)	Length (km)	complete island coverage	Height
FF04	Leg 1	7.8	03:30	399.8	Yes	Troposphere
	Leg 2	9.0	04:15	354.9	No	Troposphere
	Leg 3	10.8	05:00	432.9	Yes	Stratosphere
	Leg 4	10.8	05:45	242.3	No	Stratosphere
FF05	Leg 1	7.8	08:15	363.8	No	Troposphere
	Leg 2	9.0	08:45	366.6	No	Troposphere
	Leg 3	10.8	09:30	418.0	Yes	Stratosphere
	Leg 4	11.7	10:20	364.5	No	Stratosphere
RF16	Leg 1	12.1	07:00	443.0	No	Stratosphere
	Leg 2	12.1	07:30	510.1	Yes	Stratosphere
	Leg 3	12.1	08:30	520.5	Yes	Stratosphere
	Leg 4	12.1	09:20	552.4	Yes	Stratosphere
	Leg 5	13.0	10:05	488.7	Yes	Stratosphere
	Leg 8	12.1	11:30	463.5	Yes	Stratosphere
	Leg 9	12.1	12:15	519.2	Yes	Stratosphere

Note. Also shown is whether the flight leg is across the entire extent of the SI and in which atmospheric layer the flight leg is located.

Our study is based on the IOP 10 where the strongest low-level forcing with horizontal winds up to  $35 \text{ m s}^{-1}$  at 700 hPa occurred during DEEPWAVE. Additionally, the measured mesospheric GW activity during IOP 10 is among the two strongest detected by the Temperature Lidar for Middle Atmospheric Research (TELMA) during the entire observation period from July 2014 to November 2014 (Kaifler, Kaifler, et al., 2015).

To answer the question whether strong tropospheric forcing can cause a large-amplitude mesospheric GW response, we present a study where the propagation and evolution of GWs is investigated from the troposphere to the middle atmosphere. For this purpose, a new combination of different observations collected during the DEEPWAVE campaign is analyzed. By combining complementary observational techniques, such as in situ measurements at flight-level, radiosonde-, lidar-, and advanced mesospheric temperature mapper (AMTM) measurements, the whole vertical column of the atmosphere up to the mesosphere was observed. From these observations, GW characteristics can be derived at all altitudes up to the middle atmosphere. Mesoscale simulations from the surface to an altitude of 78 km by the Unified Model (UM) complement the measurements and give further insight in the processes of GW evolution. Additionally, forecasts and operational analyses of the Integrated Forecast System (IFS) of the European Centre for Medium-Range Weather Forecasts (ECMWF) and UM simulations are compared to lidar measurements. Using these tools, we specifically answer the following questions: Are the observed large-amplitude mesospheric waves caused by the strong low-level wind flow over the Southern Alps? Can other remote sources be excluded? If the waves are caused by topographic forcing, what prevents them from being dissipated on their way up?

The measurements and methods applied are described in section 2, and section 3 gives a detailed description of the background conditions for GW excitation and propagation during IOP 10. Section 4 presents the results of the observations starting in the troposphere and then extending into the mesosphere. A discussion of the results is given in section 5, and the conclusions in section 6 complete this study.

## 2. Instruments and Models

During DEEPWAVE's IOP 10, coordinated airborne missions were conducted across NZ's South Island (SI) by the DLR Falcon (research flights (RF) FF04 and FF05) and by the National Science Foundation/National Center for Atmospheric Research Gulfstream V (NSF/NCAR GV) (RF16) on 4 July 2014 (for details on the legs above the SI see Table 1). Figure 1 provides an overview of the vertical coverage of the different instruments and a map depicting the flight paths and locations of Haast and Lauder.

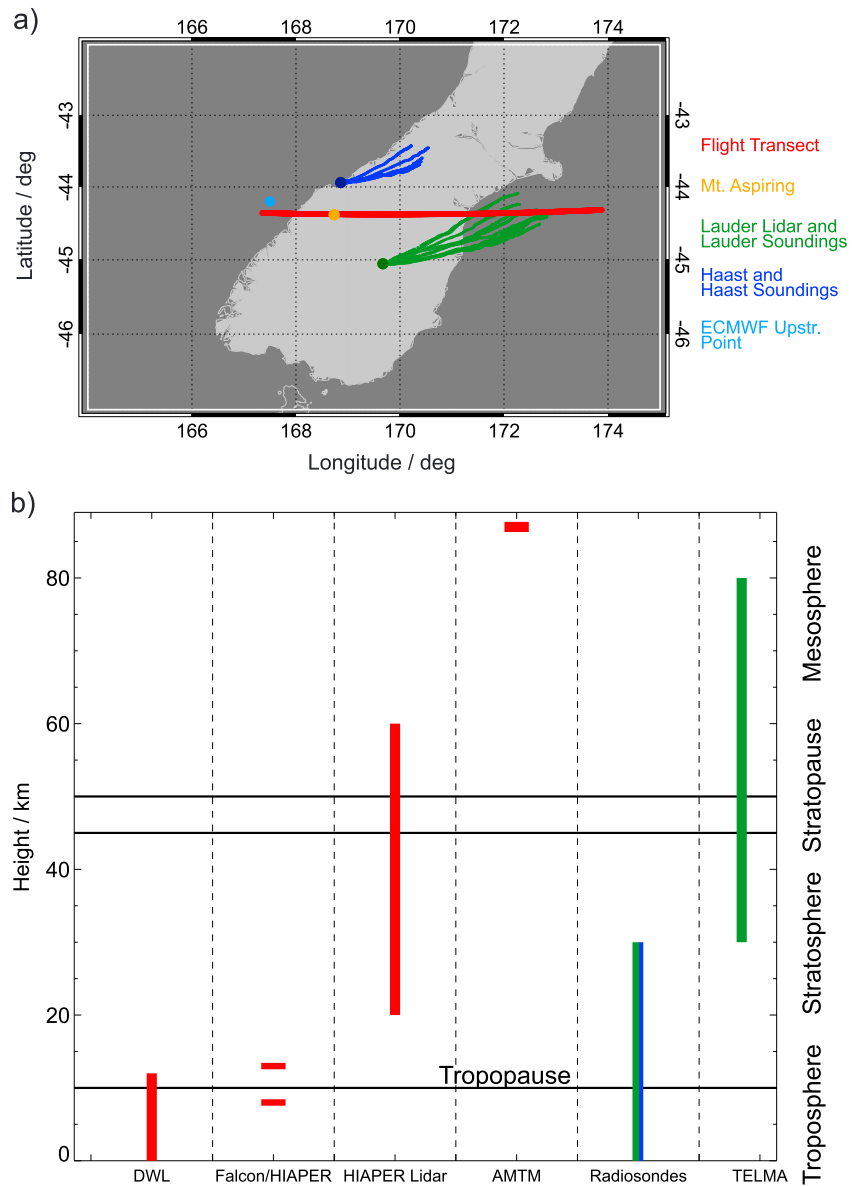


**Figure 1.** (a) Overview of the flight tracks of the research aircraft and radiosondes above the SI of NZ. The dots refer to the positions of Haast (blue), Mt. Aspiring (orange), Lauder (green), and the point used for the ECMWF upstream analysis (light blue). The lines show the flight tracks along the Mt. Aspiring transect of the research flights (red) and the radiosondes started in Haast (blue) and Lauder (green). (b) Overview of the vertical coverage of the different instruments where the color coding refers to the location of the instrument: Doppler Wind Lidar (DWL), in situ measurements of Falcon and NSF/NCAR GV (HIAPER), Rayleigh lidar mounted on NSF/NCAR GV (HIAPER Lidar), Temperature Lidar for Middle Atmospheric Research in Lauder (TELMA), radiosondes, and AMTM. The lower solid black line indicates the mean tropopause height during IOP 10 and the upper two solid black lines the position of the stratopause.

## 2.1. Measurements

### 2.1.1. In Situ Measurements

In situ measurements of wind and pressure at flight level by the DLR Falcon and NSF/NCAR GV are used to calculate leg-averaged vertical energy ( $EF_z$ ) and momentum fluxes ( $MF_x$ ,  $MF_y$ ) based on the method of Smith et al. (2008) by

$$MF_x = \frac{\bar{p}}{s} \int u' w' dx \quad (1)$$

$$MF_y = \frac{\bar{p}}{s} \int v' w' dx \quad (2)$$

**Table 2***Overview on the Measurements Uncertainties for Different Parameters of the Falcon In Situ Measurements*

	Measurement uncertainty	Random error
Static pressure	50 Pa	10 Pa
Along wind component	$0.7 \text{ m s}^{-1}$	$0.2 \text{ m s}^{-1}$
Cross wind component	$0.9 \text{ m s}^{-1}$	$0.2 \text{ m s}^{-1}$
Vertical wind ( $w$ )	$0.3 \text{ m s}^{-1}$	$0.1 \text{ m s}^{-1}$

in units (Pa) and

$$EF_z = \frac{1}{s} \int p' w' dx. \quad (3)$$

where  $\bar{\rho}$  is the mean density along the leg and  $u'$ ,  $v'$ ,  $w'$  are the perturbations of the zonal, meridional, and vertical wind components. As the horizontal integration is performed over a length  $s$  of the leg, the unit is  $\text{W m}^{-2}$ .  $MF_x$  and  $MF_y$  are the zonal and meridional components of the momentum flux vector  $\vec{MF}$ . The pressure used for calculating  $EF_z$  was hydrostatically corrected (for further information see Smith et al. (2008, 2016)). The perturbation quantities of the three wind components  $u'$ ,  $v'$ , and  $w'$  and pressure  $p'$  are calculated by subtracting linear least square fits of the respective flight level data. This approach reduces large-scale gradients due to, for example, synoptic-scale weather systems. For this study, only values of  $u'$ ,  $v'$ ,  $w'$ , and  $p'$  above land surface are taken into account. That way, effects due to upstream convection are excluded. Our results were compared to the vertical energy and momentum fluxes calculated for the DEEPWAVE overview (Fritts et al., 2016) and show the same trend and are in the same range (not shown). Detailed information on the spectral analysis of the in situ measurements is given in Appendix A. To test the linearity of the probed waves, the Eliassen-Palm relation for mountain waves between the vertical energy flux and scalar product of the vertical momentum flux and the mean horizontal wind  $\vec{U}$  was calculated according to

$$EF = -\vec{U} \cdot \vec{MF}. \quad (4)$$

The measurement uncertainties of Falcon in situ measurements are listed in Table 2 and a detailed description of this system is given in Appendix B and Bögel and Baumann (1991) and measurement uncertainties of the NSF/NCAR GV are given in Smith et al. (2016). The error estimation of the flux calculation based on DLR Falcon data, was conducted as described in Smith et al. (2016). With the same assumptions as Smith et al. (2016) regarding  $u' = 5 \text{ m s}^{-1}$ ,  $w' = 1 \text{ m s}^{-1}$ , and  $p' = 100 \text{ Pa}$  and taking into account the random error of each parameter (see Table 2), we deduce an error range from 1% to 10% for horizontal momentum and vertical energy fluxes. As the DLR Falcon random error for these parameters is the same as NSF/NCAR GV random errors, our estimated flux error is equal to the one derived by Smith et al. (2016). Thus, the DLR Falcon fluxes can be quantitatively compared to the NSF/NCAR GV fluxes.

### 2.1.2. Lidar Measurements

The downward looking Doppler Wind Lidar (DWL) on board the Falcon provides vertical time series of vertical wind with 1 s temporal resolution leading to a mean horizontal spacing of about 200 m considering an aircraft ground speed of  $\approx 200 \text{ m s}^{-1}$ . The vertical wind has a systematic error of less than  $5 \text{ cm s}^{-1}$  after correcting for the flight attitude and a vertical resolution of 100 m. The standard deviation depends on the signal-to-noise ratio and is of the order of  $20 \text{ cm s}^{-1}$ . Further instrumental details about the DWL and the corresponding wind retrieval procedures can be found in Witschas et al. (2017).

The airborne Rayleigh lidar measurements on the NSF/NCAR GV are used to examine wave propagation in the stratosphere. Bossert et al. (2015) provided a detailed description of the instrument which derives temperatures from relative density measurements in an altitude range from 25 km to 55 km. For this study, we use data with a temporal resolution of 12 s, and a boxcar averaging over six bins ( $\approx 72 \text{ s}$ ), and an altitude bin size of 300 m and boxcar averaging over six bins (1.8 km). A low-pass filter was applied to the resulting temperature perturbations with a passband of 1.8 km vertically and a passband of 72 seconds ( $\sim 17 \text{ km}$ ) horizontally in order to remove high-frequency noise. The random error of the temperature is roughly 1 K at 37 km, 5 K at 50 km, and 10 K at 60 km, respectively. We use data below 55 km, and although the error above 50 km is larger than 5 K, we consider the temperature perturbations as capable of representing the principle GW structures at these altitudes as the amplitudes in this region are with 20 K larger than the error.

**Table 3**

Overview on the Gravity Wave Spectra Captured by the Different Instruments

	$\lambda_{\text{hor}}/(\text{km})$	$\lambda_{\text{vert}}/(\text{km})$
FF in situ	$\lesssim 100$	-
FF wind lidar	0.4–200	-
GV in situ	$\lesssim 100$	-
GV lidar	$\lesssim 275$	$\lesssim 20$
TELMA	-	$\lesssim 13$
AMTM	5–300	$> 8$
Radiosondes	$\lesssim 50$	$\lesssim 13$

Ground-based Rayleigh lidar measurements by TELMA conducted at Lauder (45.0°S, 169.7°E) are utilized to characterize wave propagation from the stratosphere to the mesosphere. A description of the instrument is given by Kaifler, Kaifler, et al. (2015). In this study, we use retrieved temperature data with an effective vertical and temporal resolution of 900 m  $\times$  10 min in an altitude range of 22 to 85 km. Following Ehard et al. (2015), temperature perturbations are calculated with a fifth-order high-pass Butterworth filter with a cutoff vertical wavelength of 15 km. This limits the detection of GWs to vertical wavelengths smaller than 13 km. Details on the calculation of the gravity wave potential energy density (GWPED) are given in Ehard et al. (2017).

### 2.1.3. Radiosonde Measurements

Measurements from radiosondes launched at Haast (43.9°S, 169.0°E) and Lauder are used to derive the atmospheric background conditions for the excitation of the GWs over the Southern Alps. To analyze propagation through the troposphere and stratosphere, we focus on the soundings launched at Haast as these solely propagated

above the Southern Alps and, therefore, are not influenced by upstream or downstream processes above the ocean. During the IOP 10, a maximum altitude of 30.5 km was reached and their trajectories remained entirely above the SI. Additionally, the vertical fluctuation energy  $E_v$  related to GWs can be calculated with

$$E_v = \frac{1}{2} w^2, \quad (5)$$

where  $w$  is the vertical wind derived from the radiosonde measurements as proposed by Geller and Gong (2010).

### 2.1.4. Advanced Mesospheric Temperature Mapper Measurements

The NSF/NCAR GV Advanced Mesospheric Temperature Mapper (AMTM) measures temperatures at  $\sim 87$  km altitude over a  $\sim 120$  km  $\times$  80 km region centered near zenith, using the OH (3, 1) band emission. Additionally, two low-elevation IR imagers were mounted on each side of the plane with a field of view centered at 25° elevation angle. To extract GWs from these measurements, AMTM images are first calibrated using the star background and the coordinates of the NSF/NCAR GV, then they are projected on a linear grid to extract the GWs parameters using a 2-D fast Fourier transform algorithm. This analysis procedure has been used in previous airglow studies (Coble et al., 1998; Garcia et al., 1997). More details about this instrument and on the extraction of GWs are given in Pautet et al. (2014, 2016).

Altogether, the different measurement techniques mentioned above provide a suitable set of data to track GW propagation from surface to the mesosphere. However, the instruments cover different wavelength ranges, which are detailed in Table 3.

## 2.2. Model Configurations

To describe the synoptic situation during IOP 10, hourly forecasts and 6-hourly operational analyses of the ECMWF IFS are employed. Corresponding to a horizontal resolution of 16 km, the data of the IFS cycle 40r1 T1279/L137 are used with 137 vertical model levels and a model top at 0.01 hPa.

UM limited area simulations are used to study processes related to the propagation of the GWs to the mesosphere based on Vosper (2015), Vosper et al. (2016). The simulations use 1,100  $\times$  1,100 grid points with a horizontal spacing of 2 km, as well as 118 vertical levels and a model top at 78 km (including a sponge layer from 58.5 km). Initial conditions and lateral boundary conditions are provided by operational UM analyses, starting at 12 UTC, 3 July 2014.

Four numerical simulations with different settings of the UM were conducted in order to study the effect of topography on the wave activity in the stratosphere and mesosphere. The “control run” uses settings of the UM outlined in Vosper (2015). A second setup uses zero topography elevation and is called “flat topography.” In order to exclude the impact of changing surface conditions between water and land, NZ was drowned and the model setup is called “ocean run.” The fourth setting includes again only ocean surface but additionally convection is suppressed by removing the moisture from the interior of the model and is, therefore, referred to as “dry ocean run.”

## 3. Ambient Gravity Wave Excitation and Propagation Conditions

The meteorological situation above the SI for IOP 10 on 4 July is described with ECMWF IFS operational analyses valid at 00 UTC and 12 UTC. During IOP 10, a pronounced low-pressure system southwest of NZ together



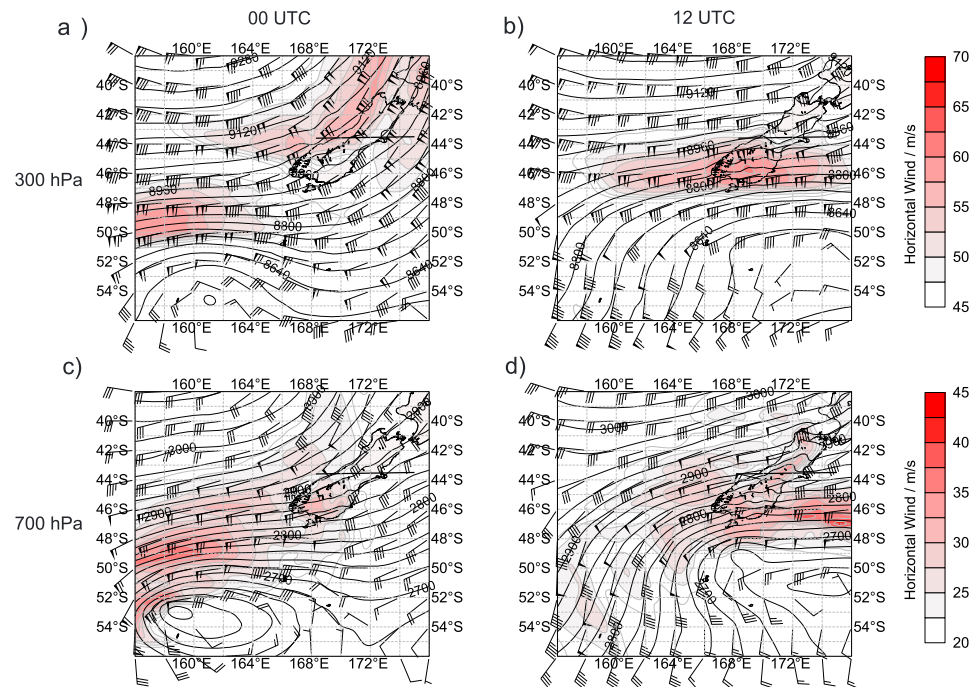


**Figure 2.** Horizontal wind ( $\text{m s}^{-1}$ , color coded) at (a and b) 300 hPa and (c and d) 700 hPa based on ECMWF operational analyses at 00 and 12 UTC, 4 July 2014. The straight black line shows the flight track above NZ. Solid black isolines are the geopotential height (m) and the wind vectors are plotted in black where short barbs represent  $2.5 \text{ m s}^{-1}$ , long barbs  $5 \text{ m s}^{-1}$  and triangles  $25 \text{ m s}^{-1}$ , respectively.

with a high pressure system northwest of NZ dominates the synoptic situation and, consequently, the excitation as well as the propagation of mountain waves in the troposphere. As the low-pressure system moves toward northeast, a zonal jet passes over NZ causing strong horizontal winds at 700 hPa (Figure 2). This pressure level is often used to represent the low-level forcing and, hereafter, will be referred to as the forcing level. Until 12 UTC, the low pressure system together with the jet approaches the SI and, consequently, the horizontal winds increase above the SI up to a maximum of  $35 \text{ m s}^{-1}$  at 700 hPa at about 09 UTC (not shown). With the passage of the low-level jet streak, not only the horizontal winds increased at forcing level but also the wind direction changed until 12 UTC (Figure 2b). While at 00 UTC the wind direction was primarily westerly, it gradually turned to a southwesterly direction by 12 UTC on 4 July, a direction present in 18% of the austral winter in 2014 (Gisinger et al., 2017). Thus, the horizontal wind direction became more parallel to the main ridges of the Southern Alps. This means that during IOP 10 the excitation of mountain waves was affected not only by a change in horizontal wind speed but also by a change in horizontal wind direction.

Between the forcing level and the tropopause at about 300 hPa, the horizontal wind increases to approximately  $50 \text{ m s}^{-1}$  (Figures 2a and 2b). Under the assumption that the dominant wave fronts are perpendicular to the mean ambient horizontal wind, a positive vertical shear favors the propagation of stationary mountain waves in the troposphere as no critical level exists in the ambient flow.

In order to determine the flow characteristics at the mountains, the nondimensional mountain height ( $\epsilon = h_m \frac{\bar{N}}{\bar{U}_{\text{norm}}}$  with the mountain height  $h_m$ , the mean static stability  $\bar{N}$  and  $\bar{U}_{\text{norm}}$  as the mean horizontal wind component normal to the Southern Alps both between 0.5 km and 3 km) is derived from radiosoundings at Haast and Lauder and plotted in Figure 3a. Here, a critical  $\epsilon$  value of  $1.4 \leq \epsilon_c \leq 1.5$  for mountain ridges (Ólafsson & Bougeault, 1996; Pierrehumbert & Wyman, 1985) is drawn to distinguish between nonlinear and linear flow regimes.  $\epsilon$  values above  $\epsilon_c$  indicate blocking resulting in flow around the mountain, while  $\epsilon < \epsilon_c$  suggests flow over the mountains which favors the excitation of mountain waves. Although the actual  $\epsilon$  values have to be taken with great care (Reinecke and Durran (2008) & Kirshbaum (2017)), it helps to classify the general flow regime and its transitional behavior during the event. In order to reflect this uncertainty,  $\epsilon$  was calculated for different mountain heights  $h_m$  ranging from 500 m to 2500 m as indicated by the error bars in Figure 3a. Obviously, lower  $h_m$  values favor flow over the mountains under the applied flow conditions.

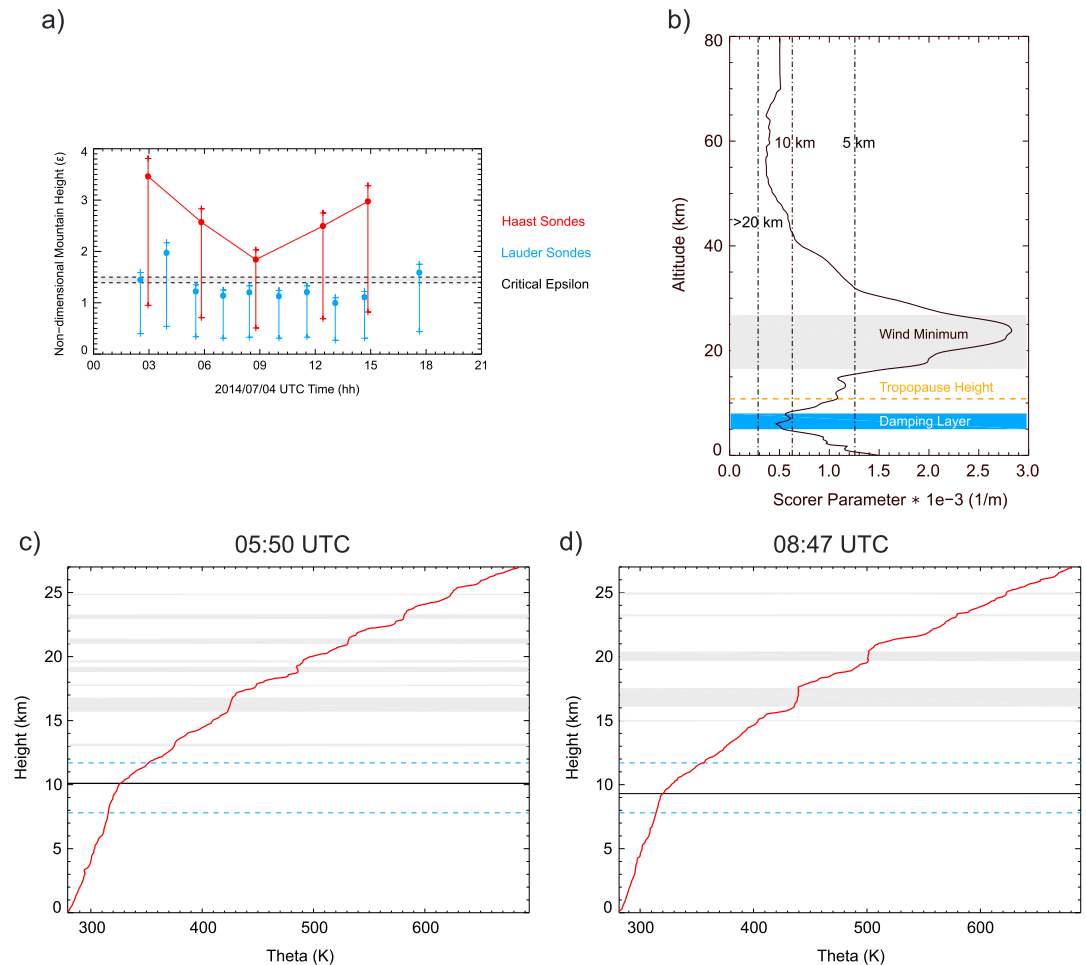


**Figure 3.** (a) Temporal evolution of the nondimensional mountain height  $\epsilon$ , derived from radiosonde measurements launched at Haast (red) and Lauder (blue). The gray shaded area shows the critical mountain height range  $\epsilon_c$ . The dots display  $\epsilon$  values calculated with the maximum altitude of the topography underneath the aircraft flight track (1,815 m) and the spread denotes  $\epsilon$  values calculated for different  $h_m$  values ranging from 500 m (minimum  $\epsilon$ ) to  $h_m = 2,500$  m (maximum  $\epsilon$ ). (b) Vertical profile of the Scorer parameter  $\ell$  from the IFS forecast valid at 09 UTC, 4 July 2014. The orange dashed line is the height of the tropopause, the gray shaded area shows the stratospheric wind minimum layer, and the blue shaded area shows the tropospheric damping layer. The vertical dash and dot lines show vertical profiles of the critical horizontal wavelengths  $2\pi/\ell$  of 5 km, 10 km and larger than 20 km. Possible breaking regions derived from vertical profiles of the potential temperature  $\Theta$ , measured by radiosondes launched at Haast at (c) 05:50 UTC and (d) 08:47 UTC. Black solid lines give the height of the tropopause and the blue dashed lines show the altitude of the flight tracks of the research flights. Gray shaded areas denote layers of  $\partial\Theta/\partial z \approx 0$  indicating turbulent mixing due to overturning waves. The range of the potential temperature gradient in these layers is between  $-0.006 \text{ K}/100 \text{ m}$  and  $0.009 \text{ K}/100 \text{ m}$ .

The observations from Haast (located upstream of the Southern Alps) differ largely from those of Lauder (located downstream the highest mountains). Overall, the Haast soundings indicate flow blocking and only a significant reduction of  $h_m$  leads to flow above the Southern Alps. In contrast, the flow regime near Lauder seems to be dominated by  $\epsilon$  values close to  $\epsilon_c$  indicating flow above the downstream mountain range. The decrease in  $\epsilon$  at 09 UTC for Haast is associated with an increase in horizontal winds  $U_{\text{norm}}$  normal to the mountain range.

The Scorer parameter ( $\ell^2 = \frac{N^2}{U^2}$  with the static stability  $N$  and  $U = \sqrt{u^2 + v^2}$ ) is used to estimate the critical horizontal wavelength ( $\lambda$ ) allowing vertical propagation of linear GWs under the given ambient atmospheric conditions (Figure 3b). The calculation of the Scorer parameter is based on ECMWF IFS forecasts for the upstream point at  $44.4^\circ\text{S}$ ,  $167.5^\circ\text{E}$ , see Figure 1. The selected  $\ell$  profile from 09 UTC shows that GWs with  $\lambda_h$  larger than 20 km should be able to propagate to the mesosphere. Wave modes with  $\lambda_h$  smaller than 20 km



are affected by the tropopause and mostly filtered before reaching the stratosphere. Results derived from  $\epsilon^2$  profiles at different but close-by time steps of the IFS are very similar.

To characterize potential regions of mountain wave breaking, we analyze vertical profiles of the potential temperature  $\Theta$  derived from Haast soundings (see Figures 3c and 3d). In  $\Theta$  profiles, expected wave breaking layers can be identified as levels where  $\partial\Theta/\partial z$  is nearly zero or even negative. During convective instability, isentropic surfaces steepen and, eventually, overturn when amplitudes become large compared to the vertical wavelength (Holton et al., 2003). This overturning is assumed to lead to turbulent mixing which is reflected by nearly vertical  $\Theta$  profiles in the soundings indicating locally neutral stratification. Such layers were identified for all soundings in the lower stratosphere between 12 km and 25 km altitude, and Figures 3c and 3d show two examples where the gray shaded regions mark layers of  $\partial\Theta/\partial z \approx 0$ . The accumulation of the mixing layers coincides with the altitude range where the horizontal wind  $U$  is minimum (Figure 3b). In the 05:50 UTC sounding, a layer depth of about 0.5–1 km can be identified, while in the 08:47 UTC sounding, the depth of two of these layers expands significantly to about 2.5 km at its maximum at an altitude of about 17 km. As the Haast sondes drifted northeast, this finding indicates nearly permanent wave breaking above the main mountain ridge between 06 UTC and 12 UTC.

## 4. Results

In the following, the results of the different measurements are presented in a way that follows the vertical propagation of the GWs starting from the troposphere up to the mesosphere.

### 4.1. Propagation in the Troposphere

The propagation through the troposphere is analyzed using DWL measurements of the vertical wind  $w$  on the example of the flight legs 2, 3, and 4 of FF04 (at around 05 UTC) and leg 4 of FF05 (at around 10:20 UTC, Figure 4a). For both flights, vertical phase lines expand throughout the troposphere, indicating mountain waves related to flow across the Southern Alps. A closer inspection of the  $w$  plots reveals that these updraft and downdrafts are rather generated by individual ridges than by the entire mountain range of the Southern Alps. During FF04 as well as FF05,  $w$  amplitudes increase from west to east: in FF04 leg 4 from 1 to 2.5 m s<sup>-1</sup> and in FF05 leg 4 from about 2 to 4 m s<sup>-1</sup>. Moreover, there is also temporal amplification between FF04 and FF05, with a maximum of 2.5 m s<sup>-1</sup> during FF04 leg 4 to a maximum of 4 m s<sup>-1</sup> during FF05 leg 4. The majority of the  $\lambda_h$  ranges between 10 and 20 km (see Figure 5). This is in concurrence with Smith and Kruse (2017), where a dominance of  $w$  power is associated with short  $\lambda_h$ . Here the observed steep phase lines in the troposphere clearly document that these waves are indeed penetrating the whole troposphere. These findings are in agreement with recent DWL observations over Northern Scandinavia by Wagner et al. (2017) and Witschas et al. (2017).

### 4.2. Influence of the Tropopause

Upper tropospheric and lower stratospheric observations of the DWL and flight-level in situ measurements from the FF05 leg 4 and RF16 leg 4 are composed to illustrate and analyze GW propagation across the tropopause. Figure 5 shows along track profiles of the vertical wind  $w$  observed by the different instruments at heights from 9.8 km to 12 km taken between 09:20 UTC and 10:20 UTC. Furthermore, the wavelet power of  $w$  is displayed for the individual profiles. The horizontal locations of updraft and downdraft agree remarkably well at all four altitudes in the vicinity of the tropopause which is located at about 10 km altitude. First of all, this reinforces the statement that the phase lines of the vertical wind are almost vertical indicating high-frequency mountain waves. Second, it reveals the stationarity of wave patterns to some degree. The dominant  $\lambda_h$  is slightly greater than 10 km. There is a drastic enhancement of the  $w$ -amplitudes from about 2 m s<sup>-1</sup> to 6 m s<sup>-1</sup> in the lower stratosphere. This enhancement is also reflected in increasing spectral power with altitude in the wavelet analysis (from about 3 m<sup>2</sup> s<sup>-2</sup> to 12 m<sup>2</sup> s<sup>-2</sup>). Additionally, significant mountain wave activity is located in the eastern part of the SI. This analysis clearly shows that mountain waves with  $\lambda_h$  larger than 10 km propagate across the tropopause into the stratosphere.

Further insight into the propagation of the mountain waves across the tropopause is obtained from the analysis of the vertical energy and momentum fluxes  $EF_z$  and  $MF$  according to equations (1)–(3). The predominantly positive  $EF_z$  values suggest a general upward propagation of the mountain waves (Figure 6a) during IOP 10. However, the values of  $EF_z$  vary highly both with time and altitude. The  $EF_z$  sampled by the DLR Falcon ranges between  $-3.8$  W m<sup>-2</sup> and  $13.2$  W m<sup>-2</sup>, while the  $EF_z$  values observed by the NSF/NCAR GV range between 0.1 and 38.1 W m<sup>-2</sup>. The maximum sampled  $EF_z$  is 38 W m<sup>-2</sup> in NSF/NCAR GV's flight leg 1

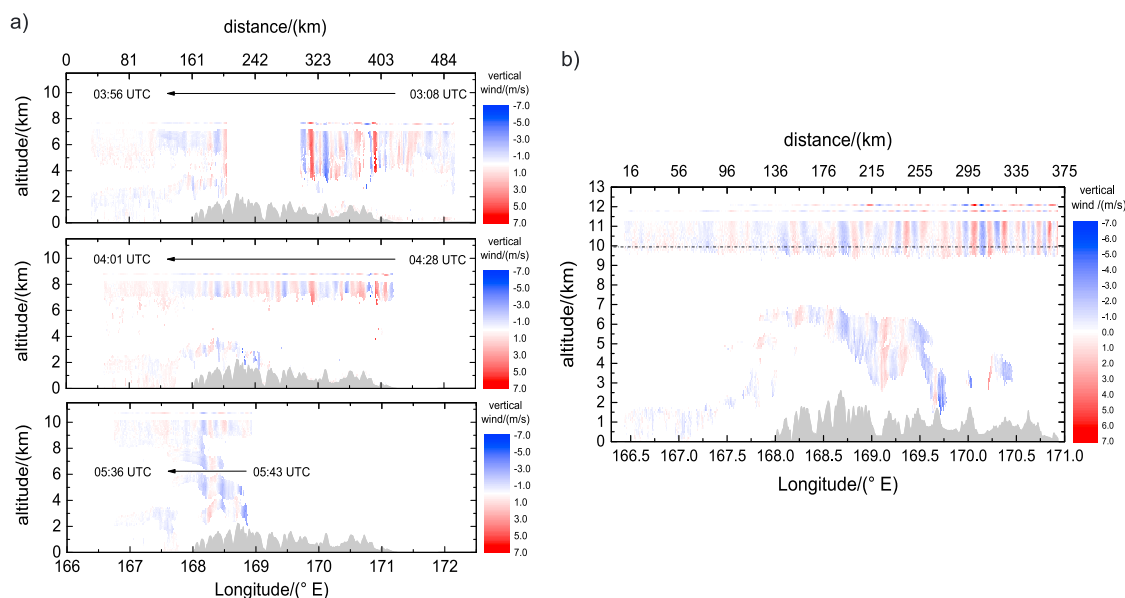


**Figure 4.** Vertical wind measurements of the DLR Falcon Doppler Wind Lidar (DWL), DLR Falcon—as well as NSF/NCAR GV—in situ measurements during (a) FF04 leg 2–4 and (b) FF05 leg 4. Horizontal axis is the longitude, vertical axis gives the altitude, and the color coding refers to vertical wind. The black dashed line gives the height of the tropopause.

and  $15 \text{ W m}^{-2}$  in Falcon's FF05 flight leg 1. These maxima are not only the maximum  $EF_z$  measured during the IOP 10 but also the maximum  $EF_z$  observed at flight levels during the complete DEEPWAVE campaign (Smith et al., 2016). As the  $EF_z$  and MF are only calculated above the land surface, our values for RF16 differ from Fritts et al. (2016) and Smith et al. (2016), where the fluxes were calculated for the complete leg length. One exception of the general positive  $EF_z$  is the FF05 leg 3 (located in the lower stratosphere), where the leg-averaged  $EF_z$  is significantly negative. Although Falcon's flight legs are located at different altitudes, they still show the same trend as the NSF/NCAR GV fluxes where the legs mostly stayed at the same altitude.

Figure 6b shows the check of the Eliassen–Palm relation (equation (4)) based on the in situ measurements of the three research flights. It reveals that the positive  $EF_z$  are highly correlated with negative MF. Thus, the flight-level vertical energy and momentum fluxes of the observed waves largely follow linear theory (Eliassen & Palm, 1961; Smith et al., 2016).

The spectral analysis of the vertical energy fluxes is presented in Figure 7 using selected legs of FF04 and FF05 of the DLR Falcon. It is striking from Figures 7a–7c that most of the vertical energy transport occurs over the eastern part of the SI in accordance with the enhanced  $w$ -amplitudes observed there (Figure 5). There, significant maxima of spectral power occur at  $10 \leq \lambda_h \leq 40 \text{ km}$ . An analysis using all cross-mountain flight legs of the three research flights is shown in Figure 7d, where the denotation of the different horizontal scales follows Smith et al. (2016). In agreement with Smith et al. (2016), our analysis reveals that for this strong forcing case, the dominant flux-carrying wavelengths are in the intermediate range between 20 and 40 km.

In FF05 leg 3 the  $EF_z$  cospectra become negative for the dominant  $\lambda_h$  (20–40 km, see Figure 7b) which explains the negative total  $EF_z$  in Figure 6 as the negative energy fluxes with values of about  $-5 \text{ W m}^{-2}$  exceed the positive energy fluxes with about  $1 \text{ W m}^{-2}$ . The observation of negative total  $EF_z$  in FF05 leg 3 is in contrast to the GV RF16, where only positive total  $EF_z$  are measured. Moreover, the negative  $EF_z$  during FF05 leg 3 is not due to only taking account the part of the flight leg above land (not shown).

#### 4.3. Propagation in the Stratosphere up to the Mesosphere

The vertical fluctuation energy related to GWs above the Southern Alps is derived from the same Haast radiosondes already shown in Figures 3c and 3d for an altitude ranging between 20 km and 26 km. This energy decreases by two third from  $1.5 \text{ J kg}^{-1}$  to  $0.34 \text{ J kg}^{-1}$ , which is an indication for an increased damping effect due to overturning waves.

Stratospheric GWs along the flight track were observed by the airborne Rayleigh lidar aboard the GV. Figure 8 shows two selected examples of temperature fluctuations  $T'$  derived from the measurements for flight legs 1

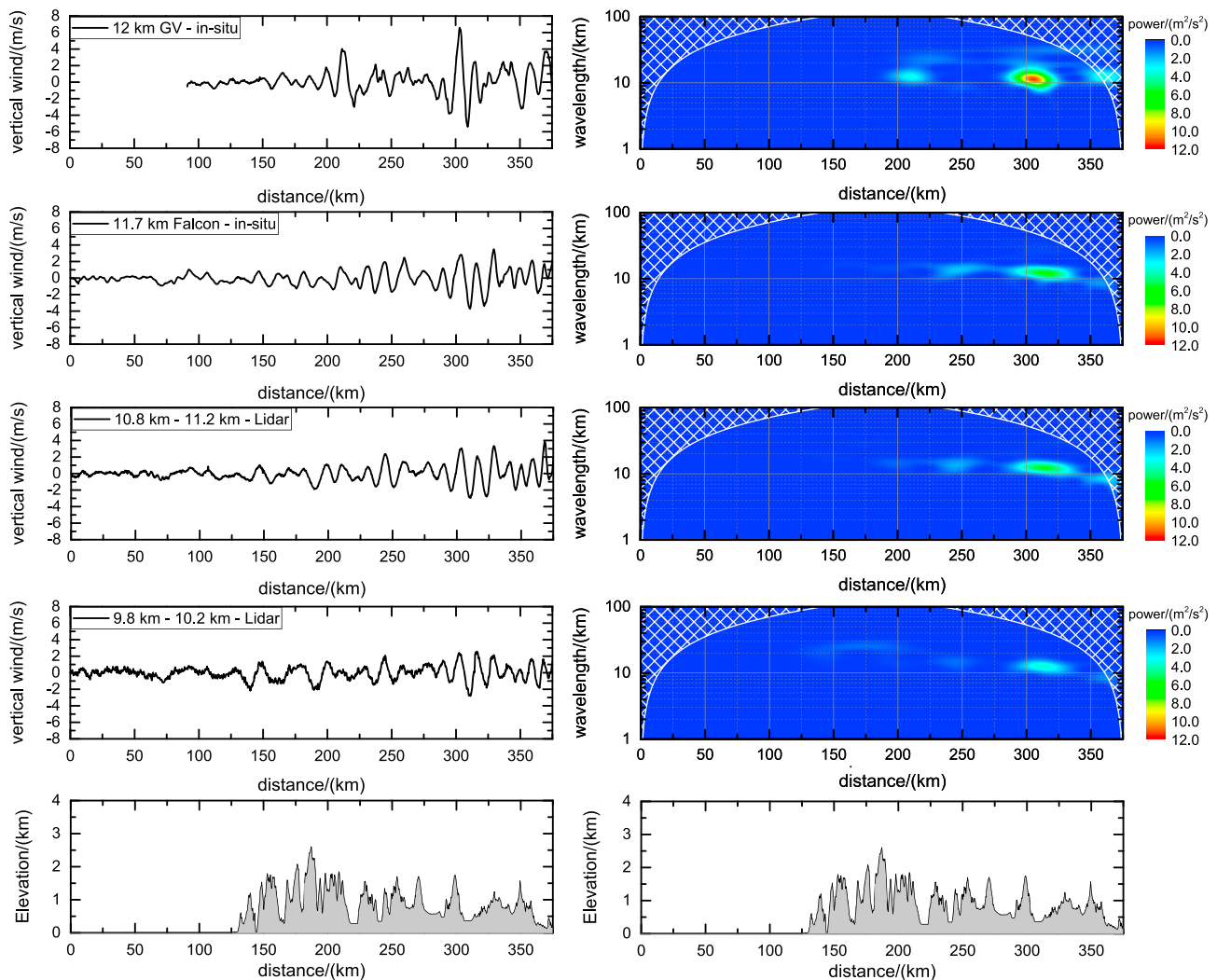


**Figure 5.** Vertical wind measurements during FF05 leg 4 of the DLR Falcon Doppler Wind Lidar (DWL), Falcon—as well as NSF/NCAR GV—in situ measurements during RF16 leg 5. Horizontal axis is the distance of the leg, vertical axis gives the (left column) vertical wind speed and (right column) wavelength, the color coding refers to power of the wavelet, whereas the shading in the wavelet shows the cone of influence. Upstream is located to the left in the figure and downstream to the right, respectively.

and 3 of RF16 together with the horizontal wind and temperature perturbations from the UM interpolated in space on both flight legs.

Below around 30 km altitude, amplitudes of the temperature perturbations are small and less coherent wave structures are present compared to higher levels in both the lidar measurements and UM simulations. Above 30 km and up to about 48 km altitude, coherent GW structures appear in the  $T'$  field of the lidar measurements with  $50 \text{ km} \leq \lambda_h \leq 80 \text{ km}$  as revealed by a wavelet analysis (not shown). The amplitudes of the observed temperature perturbations increase with altitude up to about 7 K in the region of maximum positive shear in the horizontal wind (above an altitude of about 40 km). This amplification in the maximum shear layer is very well reflected in the UM simulations where maximum amplitudes of about 6 K are simulated. Especially in the west part of the flight leg, the phase lines of the GWs are reflected in the simulations. Starting at an altitude of about 48 km the measured GW regime changes and the phase lines start to steepen in the vicinity of the core of the PNJ. In the core of the PNJ (above an altitude of 50 km), lidar measurements reveal increasing vertical wavelengths up to about  $\lambda_z \approx 10 \text{ km}$  and amplitudes exceeding 10 K. In contrast to the vertical wavelength,  $\lambda_h$  decreases in the core to about 50 km above NZ. It is striking that in this region the simulated  $\lambda_h$  matches exactly the observed one. Looking downstream the SI, GW structures in the PNJ extend horizontally in the lidar measurements, suggesting wave ducting in the PNJ. From a temporal point of view, leg 1 features coherent

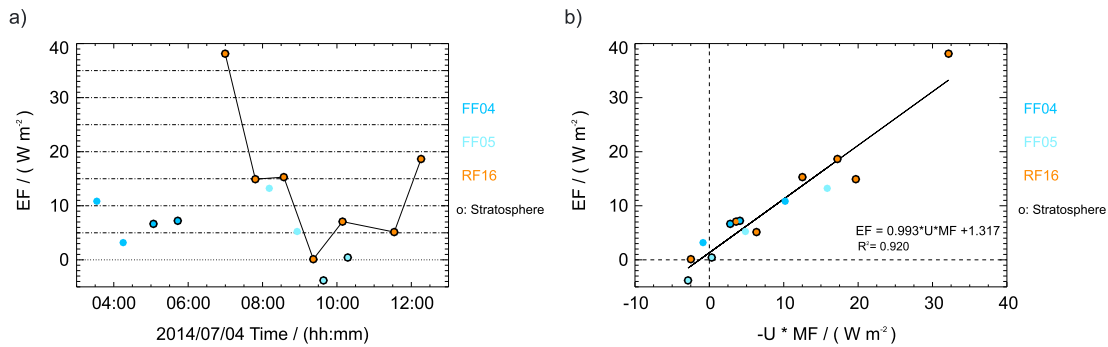


**Figure 6.** (a) Vertical energy fluxes  $EF_z$  calculated from Falcon (FF04 and FF05) and GV (RF16) in situ measurements. (b) Check of the Eliassen Palm relation based on in situ measurements of FF04, FF05, and RF16. Black circled dots refer to  $EF_z$  measured in the stratosphere.

GW structures extending across the stratosphere while the situation changes in leg 3. Here checkerboard patterns in  $T'$  evolve underneath the core of the PNJ, indicating possible wave reflection.

Additionally, nearly continuous 10 h measurements by TELMA at Lauder are analyzed. Figure 9 shows a vertical time series of temperature fluctuations at altitudes ranging from 23 km up to 79 km where the gap between 08 and 10 UTC is due to tropospheric clouds. As the measurements are at a fixed location, horizontal phase lines in Figure 9 indicate stationary gravity waves, i.e., mountain waves. In the stratosphere up to about 50 km altitude, these mountain waves with nearly stationary phase lines dominate. The slight tilt of the phase lines of about  $5^\circ$  at an altitude of  $\approx 40$  km is most likely due to transient low-level forcing or due to varying propagation conditions caused by the increase of the stratospheric wind above Lauder during the

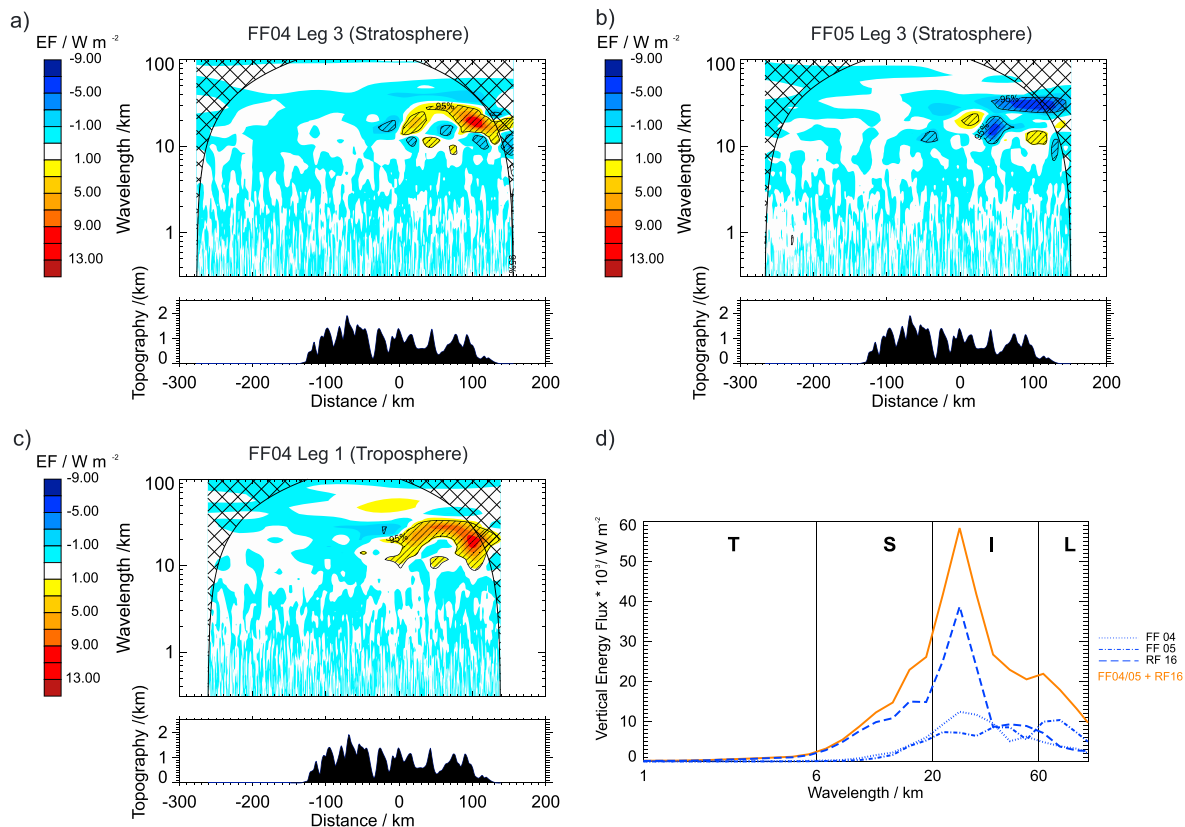


**Figure 7.** Wavelet analysis of the  $EF_z$  cospectra for flight legs located in the stratosphere ((a) FF04 leg 3, (b) FF05 leg 3), and one flight leg located in the troposphere ((c) FF04 leg 1). The hashed region refers to the cone of influence (COI), color coding is the  $EF_z$  and the 95% lines show the 95% significance level. (d) Global power spectrum for all flights during IOP 10 and sum of all flights during IOP 10 (orange). The wavelength-scale notation follows Smith et al. (2016), where "T" means "turbulence," "S" denotes "small" wavelengths, "I" refers to "intermediate," and "L" to "long" wavelengths.

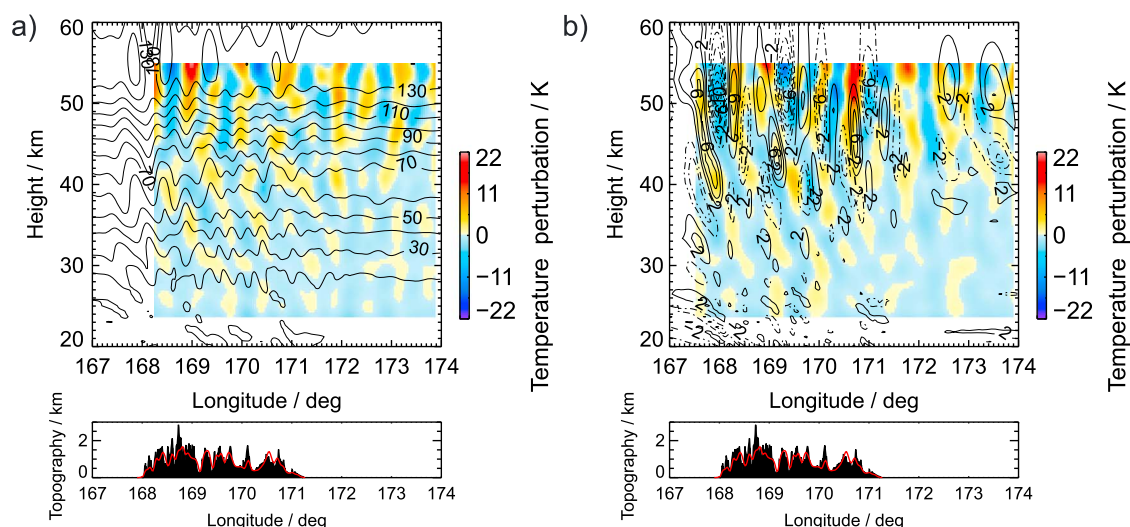


**Figure 8.** Temperature fluctuations (K, color coded) derived from temperature measurements of the GV Rayleigh lidar during (a) RF16 leg 1 and (b) leg 3. The black solid and dashed lines visualize UM results: in Figure 8a they refer to the horizontal wind ( $\text{m s}^{-1}$ ,  $\Delta U = 10 \text{ m s}^{-1}$ ) valid at 06 UTC and in Figure 8b the lines show positive (solid) and negative (dashed) temperature fluctuations (K,  $\Delta T = 2 \text{ K}$ ) valid at 09 UTC. The red topography is the UM topography.

observational period. Amplitudes increase throughout the stratopause region from about 5 K to 10 K. Between an altitude of 50 km and 60 km phase lines become disrupted, especially toward the end of the observational period. In the mesosphere above 60 km, coherent, descending phase lines indicate upward propagating non-stationary waves. In this altitude region the amplitudes increase to a maximum of about 20 K throughout the measurement period. The vertical wavelength is about 10 km throughout the vertical measurement range; however, the measurements reveal a tendency of decreasing wavelengths with altitude. Contour lines of IFS temperature fluctuations calculated in the same manner as the TELMA data reveal an astonishing geometrical alignment with the observations up to about 50 km altitude. They represent the dominant vertical GW structure with  $\lambda_z \approx 12 \text{ km}$ . Shorter waves with smaller amplitudes as they appear in the observations below 40 km are not resolved. Yet the amplitude of the temperature perturbations is underestimated by the IFS by a factor of up to about 7, in agreement with previous findings, for example, Hildebrand et al. (2017) and Le Pichon et al. (2015).

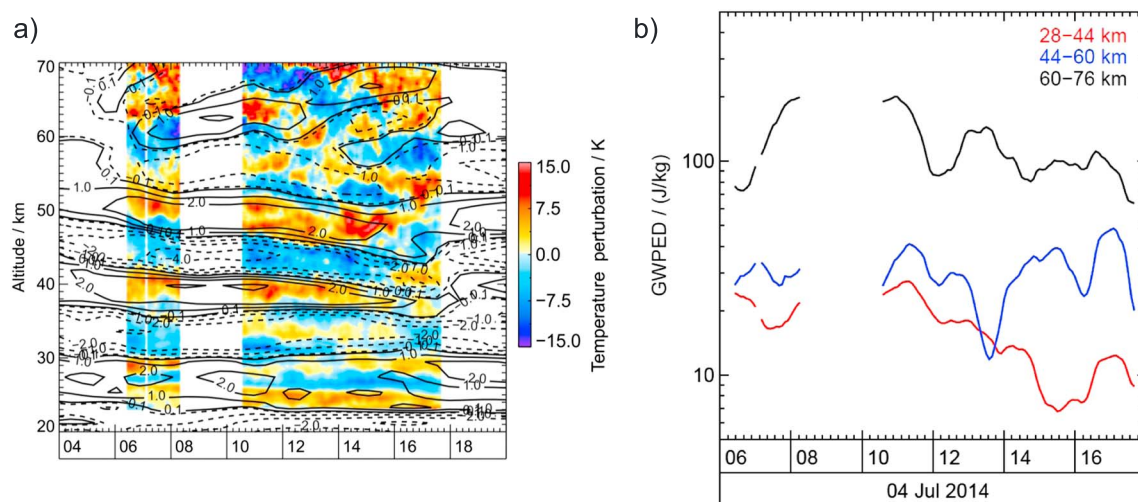


**Figure 9.** (a) Temperature fluctuations derived from measurements of the DLR Rayleigh lidar in Lauder. Horizontal axis is time, vertical axis gives the altitude and the color coding refers to temperature fluctuations. Black contours show temperature fluctuations derived from ECMWF IFS simulations interpolated in time to Lauder. (b) GWPED for stratosphere, stratopause and mesosphere derived from Lidar measurements in Lauder. The horizontal axis is time and the vertical axis denotes GWPED in a logarithmic scale.



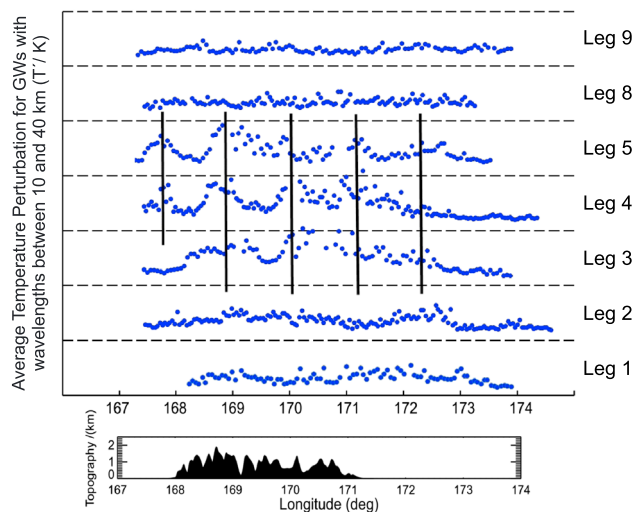


**Figure 10.** AMTM temperature perturbations along the flight track for each leg above the Southern Alps during RF16. From leg 3 to 5 stationary GWs are visible above the SI and are marked by vertical black lines.

sive legs 3, 4, and 5, i.e., from about 08:20 UTC to 10:20 UTC. At the same time visualizations of the OH airglow layer show pronounced GW activity. Earlier, between 07:22 UTC and 08:09 UTC (RF16 leg 2), small-amplitude mountain waves start to appear with  $\lambda_h$  of less than  $\approx 110$  km, cf. Figure 10, leg 2. Between 08:19 UTC and 08:50 UTC (RF16 leg 3), the GW structures become more distinct and the phase lines are located mainly above the SI. A Fourier analysis (not shown) reveals that these waves exhibit larger horizontal scales between 125 km and 130 km. However, there are also shorter structures with  $\lambda_h$  around 40 km. Between 08:59 UTC and 09:44 UTC (RF16 leg 4), the GW structures remain nearly the same, showing a little bit larger  $\lambda_h$  of about 160 km. For the next subsequent leg (09:53 UTC to 10:24 UTC, RF16 leg 5), the shorter scale GWs dominate, with  $\lambda_h$  between 30 and 50 km. After conducting two so-called trailing wave legs southeast of the SI, the GV returned after about 90 min. The AMTM detected no coherent mesospheric GWs at all along the both concluding cross-mountain legs 8 and 9, cf. Figure 10, which is the same time when the horizontal GW structures break down above 50 km altitude in the TELMA measurements.

#### 4.4. Numerical Studies With the Unified Model

The measurements undertaken during IOP 10 reveal a rather complex picture from the mountain wave excitation to the propagation into the middle atmosphere. At first glance, the local confinement of all observed waves above and downstream of the SI indicates that the large-amplitude waves observed in the mesosphere originated from the strong flow across the Southern Alps. In order to confirm this finding and to allow a detailed insight into the involved processes, limited area simulations of the UM are analyzed. Figure 12 shows vertical cross sections of  $T'$ ,  $w$ , and  $\Theta$  as well as horizontal wind along the Mt. Aspiring transect for the different model runs valid at 09 UTC.

In the control run (Figures 12a–12c), the vertical wind in particular reveals mountain waves excited at the Southern Alps which extend across the tropopause. The simulated vertical wind amplitudes of about  $3 \text{ m s}^{-1}$  are in the same range compared to the DWL measurements. Above the tropopause, their phase lines tilt upstream due to the negative horizontal wind shear and  $\lambda_h$  of about 30 km (Figure 12b). Between an altitude of 15 km and 30 km, GW amplitudes are strongly reduced due to local wave breaking and turbulent mixing. As in the observations, the simulated breaking layer is associated with the stratospheric wind minimum (Figure 12c). Between 25 km and 35 km altitude, the amplitudes in  $T'$  are with up to  $\sim 2 \text{ K}$  in the same range as the airborne Rayleigh lidar measurements with about 2.5 K. Above the breaking layer,  $w$  amplitudes amplify and the horizontal wind increases up to the stratopause (Figures 12b and 12c). In concert with the GV lidar measurements, a checkerboard pattern in both the temperature fluctuations and the vertical wind is simulated underneath the core of the PNJ with an approximate  $\lambda_h$  of 60 km. This wavelength compares well with the GV lidar measurements at an altitude of 45 km where the dominant  $\lambda_h$  ranges between 50 km and 65 km. At the core of the PNJ between 50 and 65 km, phase lines become nearly vertical with a  $\lambda_h$  of about

The GWPED derived from TELMA measurements as a running mean over 1 h is displayed in Figure 9b for three middle atmospheric layers representing the stratosphere, stratopause and mesosphere. In general, and as expected, the GWPED increases with altitude attaining values of about  $200 \text{ J kg}^{-1}$  at the uppermost levels, compared to the lower level where values do not exceed  $50 \text{ J kg}^{-1}$ . The decrease of GWPED down to about  $10 \text{ J kg}^{-1}$  at 28 to 44 km altitude after 14 UTC goes along with the fading temperature fluctuations as shown in Figure 9a. In the mesosphere, GW activity varies significantly with respect to time. A distinct increase of about  $180 \text{ J kg}^{-1}$  between 06 and 08 UTC is followed by a decrease of about the same amount 4 h later. Afterward, GWPED values fluctuate around  $100 \text{ J kg}^{-1}$  in the mesosphere and about  $30 \text{ J kg}^{-1}$  in the stratopause region. Whereas GWPED is decreasing in the mesosphere and stratosphere up to 44 km, wave energy seems to be continuously large inside the PNJ, i.e., in the height region between 44 and 60 km. This finding agrees with the large temperature fluctuations found in the airborne lidar data along the flights tracks, see Figure 8.

To obtain more insight on the mesospheric GW activity at about 87 km altitude along the flight track, AMTM measurements are analyzed and displayed in Figures 10 and 11. Temperature fluctuations derived from the AMTM reveal nearly stationary structures above the SI during the succes-

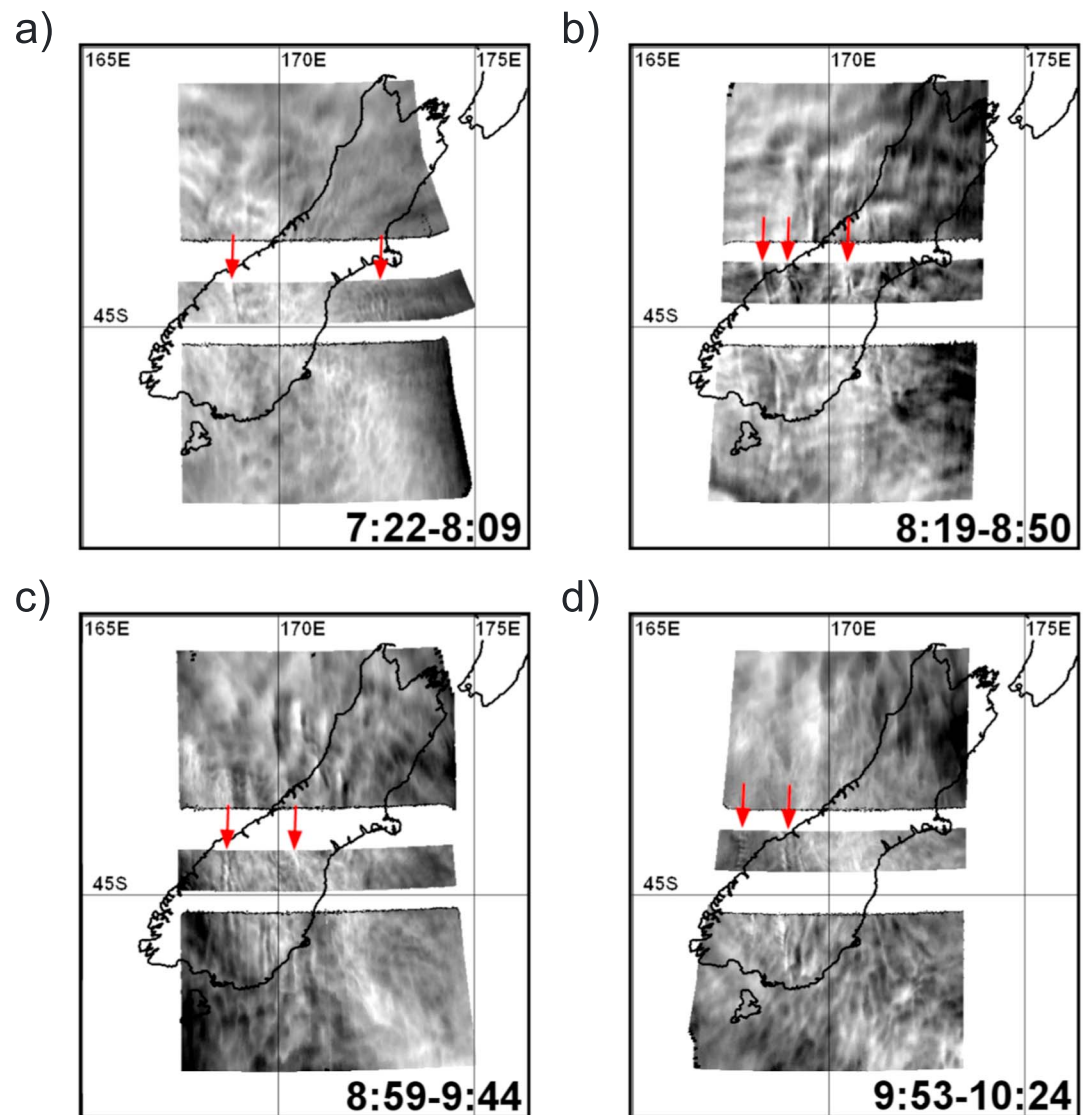


**Figure 11.** (a–d) Airglow images at 87 km altitude during RF16 leg 2–5; black lines show the coastline of the SI of NZ. Especially in leg 3 and 4 GWs with different  $\lambda_h$  are present above the SI (Figures 11b and 11c). After leg 5 no coherent wave structures were observed. Red arrows highlight the position of gravity waves.

70 km and maximum amplitudes of  $5 \text{ m s}^{-1}$  in the vertical wind and about 10 K in the temperature fluctuations. Here the  $T'$  amplitudes tend to be underestimated by the UM, while the simulated vertical structure of the phase lines confirms largely the airborne lidar observations. In contrast to the observations, the simulated wave structures are not confined to the SI alone in the control run. Especially, the vertical wind extends both upstream and downstream of the SI, but with reduced amplitudes. With respect to time, the principal wave structures in the mesosphere remain nearly stationary for other time steps than 09 UTC (not shown).

The two sensitivity runs “flat topography” and “ocean surface” aim at clarifying that the topography is the dominant excitation mechanism of the observed mesospheric gravity waves. Additionally, the “dry ocean surface” run excludes all diabatic processes related to the phase changes of water vapor. All three simulations reveal mesospheric GWs, however, with much reduced amplitudes in both  $w$  (Figures 12e, 12h, and 12k) and  $T'$  (Figures 12d, 12g, and 12j). Interestingly, the flat topography run shows  $w$  amplitudes up to  $3 \text{ m s}^{-1}$  and  $T'$  amplitudes of 4 K inside the core of the PNJ at about 50 km altitude. It must be noted that the PNJ also has a reduced thermal stability (cf. isentropic surfaces in Figure 12h or 12k) which does not support damping of vertical oscillations. This indicates that the horizontal variation of the surface roughness from ocean to land alone might generate small disturbances in the flow field which can propagate up, amplify, and excite

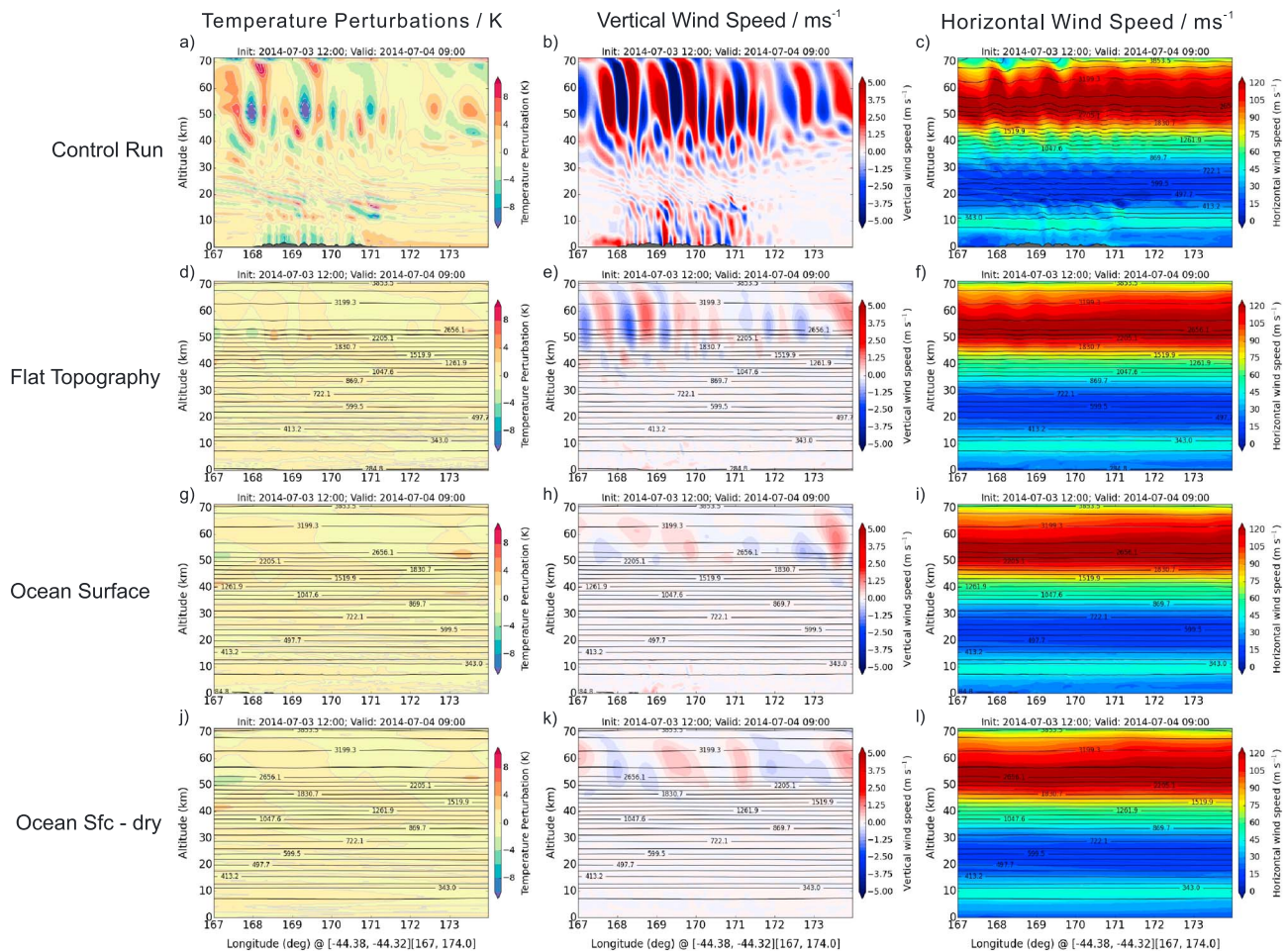


**Figure 12.** Vertical cross sections of the (a, d, g, and j) temperature fluctuations, (b, e, h, and k) vertical wind, and (c, f, i, and l) horizontal wind along the flight track based on limited area UM simulations valid at 09 UTC. The rows show the results of the four different numerical setups. The first row gives the output of the control run (Figures 12a–12c), the second of the flat topography run (Figures 12d–12f), the third of the ocean surface (Figures 12g–12i), run and the bottom row of the dry ocean surface run (Figures 12j–12l), respectively.

certain wave modes in the mesosphere. Using only water surface (run ocean surface) reduces the mesospheric  $w$  amplitudes further to values less than  $1 \text{ m s}^{-1}$  which are nearly the same as in the dry simulation (Figures 12h and 12k). Here the  $T'$  amplitudes are reduced so strongly that no wave structures are visible anymore (Figure 12 j). Although  $w$  perturbations in the PNJ are present in all simulations, the large amplitude, the shorter  $\lambda_h$ , and finally, the qualitative agreement with the airborne lidar measurements suggest the flow across the Southern Alps as the dominant GW source. The reason for the appearance of the wavy disturbances in the PNJ might be imbalance in the initialization or other numerical artifacts which manifest themselves as mesospheric oscillations.

## 5. Discussion

Vertical phase lines of vertical wind observed by the DWL in both DLR Falcon flights (Figure 4) as well as in the UM simulations (Figure 12) suggest that high-frequency GWs are excited by strong flow across the rugged terrain of the Southern Alps. Their  $\lambda_h$  between 10 km and 20 km point to single mountain peaks rather than the complete range of the Southern Alps as dominant sources. The Fourier analysis of the digital orography along the Mt. Aspiring cross section also reveals peaks in the spectral power at around 10 km roughly corresponding to the observed  $\lambda_h$  in the troposphere (not shown). In both DLR Falcon research flights FF04 and FF05  $w$  amplitudes of the mountain waves increase to the east of the SI by  $1\text{--}2 \text{ m s}^{-1}$ . This is in concurrence with the comparative analysis of the nondimensional mountain height  $\epsilon$  (Figure 3a) which indicates flow blocking



upstream of the SI and reduced mountain wave activity in this area. On the other hand, flow over mountains dominates in the east of the SI leading to larger amplitude waves above these mountains.

The observed mountain waves penetrate mainly without dissipation throughout both the troposphere and the tropopause. Analysis of the Scorer parameter (Figure 3b) reveals that long and intermediate GWs with  $\lambda_h \gtrsim 10$  km are able to propagate through the lower atmosphere without complete reflection. Although solely based on upstream IFS profiles, this estimate confirms the vertical wind measurements of the DWL and in situ measurements of the DLR Falcon and NSF/NCAR GV (see Figure 5), which show stationary wave patterns across the tropopause with  $\lambda_h \approx 10$ –20 km. In the lower stratosphere, the amplitudes of the mountain waves increase with altitude due to decreasing density. The validity of the Eliassen–Palm relation derived from aircraft in situ measurements at flight levels below and above the local tropopause (Figure 6b) further indicates nearly linear wave propagation across the tropopause. Also, the high-resolution numerical simulations reveal nearly stationary, nonbreaking wave patterns stretching across the tropopause up to the lower stratosphere. However, the simulated  $\lambda_h \approx 30$  km are larger than those of the DWL measurements. This might be an effect of the smoother model topography compared to the real topography which leads to broader mountains and thus larger  $\lambda_h$  (Figure 8). As in the tropospheric DWL observations, the in situ aircraft measurements also show that the main mountain wave activity is concentrated in the eastern part of the SI. The dominating  $\lambda_h$  of the flux-carrying waves calculated from the DLR Falcon observations are in the intermediate scale of  $20 \text{ km} \leq \lambda_h \leq 60 \text{ km}$ , Figure 7. These findings confirm the results of Smith et al. (2016) whose analysis is based on the NSF/NCAR GV data only.

Above the tropopause, the negative vertical shear of the ambient flow leads to upstream tilted phase lines (Figure 12). Here the mountain waves propagate up into the stratospheric wind minimum located between 15 km and 30 km altitude (Figure 12c). As density decreases with altitude, wave amplitudes increase exponentially with height. Furthermore, the wave-induced perturbations of the horizontal wind attain similar magnitudes as the slow background wind. In the case of mountain waves with zero ground-based phase speed, convective instability is likely to occur as the ratio of perturbation to background wind approaches unity (cf. Fritts & Alexander, 2003, equation (58)). Although no critical layer for stationary mountain waves exists in the ambient flow, widespread wave breaking occurs in the stratospheric wind minimum. There, the Haast radiosondes detected several narrow layers showing turbulence in this region, above the Southern Alps (Figures 3c and 3d). Turbulent spots such as these are also resolved in the UM simulations as regions where isentropes locally steepen indicating wave overturning and turbulent mixing. As a consequence, amplitudes of the vertical wind reduce significantly by about  $4 \text{ m s}^{-1}$  (Figures 12a and 12b). Kruse et al. (2016) refer to this minimum wind layer as the “valve layer,” and it was observed in several IOPs during DEEPWAVE. Such a layer was also found in middle and upper (MU) atmosphere-radar measurements in the lower stratosphere above Japan (Sato, 1990) and a numerical study revealed that GWs break in this region due to convective instability (Satomura & Sato, 1999). Another remote sensing observation of such a breaking process was provided by Dörnbrack et al. (2002), their Figure 5. Consequently, the wave breaking leads to turbulent mixing which enhances the effective viscosity of this layer. These local breaking regions act as an obstacle to the surrounding flow and further decelerate the ambient horizontal flow. As a result, upward and downward propagating secondary waves are generated in this layer, which is shown in simulations by Satomura and Sato (1999). The observed negative  $EF_z$  values along leg 3 in FF05 (Figure 7b) could be caused by such downward propagating secondary waves. However, our and previous numerical studies suggest that not all waves are damped and dissipated in this layer and, therefore, primary mountain waves leak through the valve layer (Satomura & Sato, 1999).

Above the breaking region, GV lidar measurements reveal upward propagating mountain waves with amplified amplitudes of about 10 K over NZ (Figure 8). Supporting this, both the UM control run (Figure 12a–12c) and the ground-based Rayleigh lidar measurements reveal enhanced wave amplitudes above the valve layer in a band of positive vertical shear of the ambient horizontal wind. Underneath the PNJ, a checkerboard pattern in the vertical wind indicating partially reflected mountain waves was observed by the airborne lidar as well as simulated by the UM. Quantitatively, the GWPED derived from TELMA measurements does not increase exponentially across the stratosphere (Figure 9b). As the GWPED is a mass-dependent parameter, it increases exponentially with altitude due to the decreasing density for a purely vertically propagating GW with uniform background wind. Deviations from this profile point either to dissipation or to reflection in the respective atmospheric layers. Also, the phase lines between 50 km and 60 km in the temperature perturbations derived from TELMA measurements show broken incoherent pattern (Figure 9) indicating either reflection or

dissipation between 12 and 18 UTC. This period corresponds exactly to the times when the airborne AMTM measurements show fading wave amplitudes in the mesospheric OH airglow layer. In the region of the PNJ (at an altitude of  $50 \text{ km} < z \leq 60 \text{ km}$ ), airborne lidar measurements as well as UM simulations reveal nearly vertical phase lines and corresponding large vertical wavelengths similar to the patterns found in the troposphere. These GW structures are also present downstream of the SI in both the simulations and measurements, thus suggesting that mountain waves are being trapped in the PNJ. Above the PNJ, horizontal wind decreases with altitude (Figure 12) and the mountain waves again lean in the surrounding flow, leading to upstream tilted phase lines, indicating upward propagation (Figure 9). At 87 km, AMTM measurements show nearly stationary mountain waves above the SI for about 2.5 h (Figure 10). The airglow images show GW structures that are variable with time with respect to their  $\lambda_h$  (Figure 11). With a ground-based phase speed equal to zero, the longer waves with  $\lambda_h \approx 100 \text{ km}$  can be attributed to the tropospheric forcing. Assuming a mean background wind of about  $40 \text{ m s}^{-1}$ , it takes hydrostatic GWs with  $\lambda_h \approx 50 \text{ km}$  approximately 2.5 h to propagate from the surface to an altitude of 87 km. This means that these GWs are excited around 05–06 UTC. Longer GWs with  $\lambda_h \approx 100 \text{ km}$ , on the other hand, need about 4 h to propagate to this altitude, suggesting a generation time around 03–04 UTC. The series of UM simulations with and without topography confirms the AMTM measurements and shows that strong tropospheric forcing causes mesospheric GWs.

The appearance of the large-amplitude mountain waves observed in the stratosphere and mesosphere raises the question of which processes do prevent them from dissipating? A possible hypothesis is that the valve layer allows a leakage of wave modes into the upper stratosphere. Its dampening effect reduces the amplitudes but does not eliminate the mountain waves. The UM control run reveals that the permeability of the valve layer seems to be influenced by the low-level forcing. This is logical as the stronger the forcing, the larger the amplitudes of the generated mountain waves, and the more likely they break due to convective instability. When the forcing is less strong, amplitudes become smaller and the GWs can propagate to higher altitudes without breaking. This implies that the valve layer is most impermeable during strong forcing conditions. Haast radiosonde measurements confirm the simulation with respect to the time/forcing dependence of the valve layer above the Southern Alps (Figures 3c and 3d) in two ways: on the one hand the layer thickness of the turbulent layers and on the other hand with the vertical fluctuation energy related to GWs above an altitude of 20 km. While at the 05:50 UTC sounding the turbulent layers only extend about 0.5–1 km in the vertical, the thickness of the turbulent layers increase to about 2 km in the 08:47 UTC sounding (Figures 3c and 3d). Additionally, the energy passing through these turbulent layers decreases by two thirds between the two soundings. Thus, the valve layer controls the upward propagation of mountain waves into the mesosphere, as delineated by the decreasing mesospheric GW activity after 10:30 UTC coinciding with enhanced turbulence in the stratospheric wind minimum. On the other hand, GW propagation might also be affected in the vicinity of the local tropopause. As it turned out, the  $EF_z$  has the lowest values when the forcing is maximum and secondary upward and downward propagating waves are generated in the valve layer. The superposition of primary upward and secondary downward propagating waves could lead to cancelation effects between the positive and negative  $EF_z$  values resulting in decreased net  $EF_z$  at flight level. However, this hypothesis needs further testing with idealized simulations.

## 6. Conclusions

This study raised the question whether strong tropospheric forcing did cause large-amplitude gravity waves in the mesosphere. To answer this question, we combined and analyzed a comprehensive data set consisting of aircraft data, airborne and ground-based lidar measurements, radiosonde, and advanced mesospheric temperature mapper data. In contrast to former studies which only concentrated on specific altitude layers (e.g., Bougeault et al., 1997; Kaifler, Kaifler, et al., 2015; Pautet et al., 2016; Smith et al., 2009, 2016; Woods & Smith, 2010) our new approach allows for the observation of gravity waves from the troposphere to the mesosphere as it combines instruments that completely cover this atmospheric range.

Although recent studies revealed that strong mesospheric gravity wave activity is connected to low or moderate tropospheric forcing (e.g., Fritts et al., 2016; Kaifler, Kaifler, et al., 2015), our data show evidence that strong tropospheric forcing can also result in large-amplitude mesospheric mountain waves. There are three essential ingredients for their deep propagation: the nearly linear propagation across the tropopause, the leakage through the stratospheric wind minimum, and their amplification in the PNJ. During DEEPWAVE's IOP 10 mountain waves were generated by strong low-level flow across the Southern Alps and attained the largest lower stratospheric vertical energy fluxes measured during the whole field campaign. In the tropopause



region, partial reflection influenced the vertical propagation mainly for mountain waves with  $\lambda_h \lesssim 10$  km. Horizontally longer waves with  $\lambda_h > 10$  km propagated into the lower stratosphere. There, the stratospheric minimum wind layer (background wind speed  $\approx 10 \text{ m s}^{-1}$ ) facilitated convective instabilities, wave breaking, and the generation of secondary waves. However, not the complete wave spectrum was filtered or eliminated by this valve layer and leaking mountain waves propagate upward. Their amplitudes amplified and the waves were trapped in the PNJ. At the stratopause region the situation becomes challenging as downward propagating waves were observed, generated either by reflection or by the strong wind shear of the PNJ. Still, stationary mountain waves are present in the AMTM measurements with  $\lambda_h \approx 100$  km. The observed large amplitudes are likely due to the effect of decreasing density or reduced thermal stability above the stratopause. The direct link between the observed mesospheric mountain waves and the strong tropospheric forcing raises the question why the waves were neither totally dissipated nor horizontally refracted. First, the valve layer attenuates the mountain wave amplitudes and also allows modes to leak through the stratospheric wind minimum. Second, the location of the PNJ directly above NZ facilitated a dominant vertical propagation of the mountain waves.

Especially complicated situations as the presented case of DEEPWAVE's IOP 10 show that a combination of data covering the complete altitude range from troposphere to mesosphere was necessary to describe the involved processes. High-resolution numerical simulations with domain tops in the mesosphere are essential for the physical understanding and the testing of hypotheses with respect to the sources of the observed gravity waves.

## 7. Data Availability

Generally, DEEPWAVE data are stored and maintained by NCAR and are available at [https://www.eol.ucar.edu/field\\_projects/deepwave](https://www.eol.ucar.edu/field_projects/deepwave). Digital Object Identifiers (DOIs) are assigned to some data sets: (i) GV insitu measurements: <https://doi.org/10.5065/D66Q1V8B>; (ii) Haast radiosondes: <https://doi.org/10.5065/D6Z31x1N>; (iii) Lauder radiosondes: <https://doi.org/10.5065/D62V2DHM>; and (iv) TELMA: <https://doi.org/10.5065/D67P8WRN>

## Appendix A: Wavelet Analysis of In Situ Measurements

The spectral analysis of the  $EF_z$  was conducted by means of the wavelet analysis (Torrence & Compo, 1998). Following Woods and Smith (2010), the cospectrum of  $EF_z$  was calculated by

$$\widetilde{EF}_n(s_j) = \Re\{\tilde{P}_n(s_j)\tilde{W}_n^*(s_j)\} \quad (\text{A1})$$

where an appropriate scaling assures the unit of  $\widetilde{EF}_n(s_j)$  being  $\text{W m}^{-2}$  and  $\Re$  denotes the real part. The quantity  $\tilde{P}_n(s_j)$  is the wavelet transform of the pressure perturbation with the wavelet scale  $s_j$  and  $\tilde{W}_n^*(s_j)$  denotes the complex conjugate of the wavelet transform of the vertical wind perturbation. In order to make the  $EF_z$  in wavelet space ( $\widetilde{EF}$ ) comparable to the total  $EF_z$  (equation (3)), the wavelet analysis in section 4 shows the reconstructed  $\widetilde{EF}$  given by

$$EF_z(n, j) = \frac{\Delta j \Delta x}{C_\delta} \cdot \frac{\widetilde{EF}_n(s_j)}{s_j} \quad (\text{A2})$$

where  $\Delta j$  is the wavenumber increment,  $C_\delta = 0.776$  represents the reconstruction factor (see also Torrence and Compo, 1998), and  $\Delta x$  refers to the increment of the equally spaced grid along the flight track. The cospectrum  $\widetilde{EF}_n(s_j)$  is a two-dimensional field with the indices  $n$  referring to the flight track and  $j$  to the scale. The unit of the reconstructed vertical energy flux  $EF_z(n, j)$  is again  $\text{W m}^{-2}$ .

### A1. Aircraft Measurement Uncertainties

Giez et al. (2017) describe the latest quality verification with a trailing cone system performed in 2011. The difference of the reference pressure and the static pressure measured with the noseboom is below  $\pm 25$  Pa for all the test points between Mach number 0.25 and 0.8. To estimate the error propagation, the scheme described in Mallaun et al. (2015) was used. White noise was added to the raw signals with an amplitude equal to the individual measurement uncertainty of the target parameter. The wind calculation was performed with the biased raw signals. Finally, the propagated error of the derived quantities was calculated from the white noise peak in a cross correlation analysis.

For the calculation of the fluxes by means of equations (1)–(3), the measurement uncertainties were significantly reduced, as a random error of the signals gives the appropriate error estimation (Smith et al., 2016). Any sensor bias was eliminated and the short flight legs without significant changes of height and direction reduce the error sources (e.g., sensor drift, temperature dependency, and alignment error of the laser gyro). Meischner et al. (2001) estimated the random error of the Falcon basic data for turbulence measurements. They estimated the quantization error to be about  $0.01 \text{ m s}^{-1}$  for the wind components perpendicular to the flight direction and  $0.03 \text{ m s}^{-1}$  for the longitudinal component. In 2014, a new data acquisition system (ACRA SSR/CHS/001 and analog device ACRA KAD/ADC/112) was installed with increased resolution of the analog devices (i.e., from formerly 14 bits to 16 bits). The expected random error is less than the measurement uncertainty, but higher than the quantization error. For the vertical wind it is below  $0.1 \text{ m s}^{-1}$  and for the horizontal components below  $0.3 \text{ m s}^{-1}$ .

## Acknowledgments

Part of this research was funded by the German research initiative "Role of the Middle Atmosphere in Climate (ROMIC/01LG1206A)," by the German Ministry of Research and Education in the project "Investigation of the life cycle of gravity waves (GW-LCYCLE)," and by the Deutsche Forschungsgemeinschaft (DFG) via the Project MS-GWaves (GW-TP/DO 1020/9-1 and PACOG/RA 1400/6-1). Access to the ECMWF data was possible through the special project "HALO Mission Support System." The UM simulations were conducted with the MONSOON system, a collaborative facility supplied under the Joint Weather and Climate Research Programme, a strategic partnership between the Met Office and the Natural Environment Research Council. M. Bramberger wants to thank Kaoru Sato and Ron Smith for insightful discussions and Sonja Gisinger for help with radiosonde data analysis. The developments of the GV instruments were funded by the NSF grants AGS-1061892 (USU) and AGS-1261619 (GATS). The DEEPWAVE campaign was sponsored by the NSF grants AGS-1338666 (USU) and AGS-1338646 (GATS). DEEPWAVE data are stored and maintained by NCAR and are available at [https://www.eol.ucar.edu/field\\_projects/deepwave](https://www.eol.ucar.edu/field_projects/deepwave). We thank three anonymous reviewers for insightful comments and suggestions that have contributed to improve this paper.

## References

- Bögel, W., & Baumann, R. (1991). Test and calibration of the DLR Falcon wind measuring system by maneuvers. *Journal of Atmospheric and Oceanic Technology*, 8, 5–18. [https://doi.org/10.1175/1520-0426\(1991\)008<0005:TACOTD>2.0.CO;2](https://doi.org/10.1175/1520-0426(1991)008<0005:TACOTD>2.0.CO;2)
- Bossert, K., Fritts, D. C., Pautet, P.-D., Williams, B. P., Taylor, M. J., Kaifler, B., ... MacKinnon, A. D. (2015). Momentum flux estimates accompanying multiscale gravity waves over Mount Cook, New Zealand, on 13 July 2014 during the DEEPWAVE campaign. *Journal of Geophysical Research: Atmospheres*, 120, 9323–9337. <https://doi.org/10.1002/2015JD023197>
- Bougeault, P., Benec, B., Bessemoulin, P., Carissimo, B., Clar, A. J., Pelon, J., ... Richard, E. (1997). PYREX: A summary of findings. *Bulletin of the American Meteorological Society*, 78(4), 637–650. [https://doi.org/10.1175/1520-0477\(1997\)078<0637:PASOF>2.0.CO;2](https://doi.org/10.1175/1520-0477(1997)078<0637:PASOF>2.0.CO;2)
- Coble, M., Papen, G. C., & Gardner, C. S. (1998). Computing two-dimensional unambiguous horizontal wavenumber spectra from OH airglow images. *IEEE Transactions on Geoscience and Remote Sensing*, 36(2), 368–382. <https://doi.org/10.1109/36.662723>
- Dörnbrack, A., Birner, T., Fix, A., Flentje, H., Meister, A., Schmid, H., ... Mahoney, M. J. (2002). Evidence for inertia gravity waves forming polar stratospheric clouds over Scandinavia. *Journal of Geophysical Research*, 107(D20), 8287. <https://doi.org/10.1029/2001JD000452>
- Dunkerton, T. J. (1984). Inertia-gravity waves in the stratosphere. *Journal of Atmospheric Sciences*, 41(23), 3396–3404. [https://doi.org/10.1175/1520-0469\(1984\)041<3396:WITS>2.0.CO;2](https://doi.org/10.1175/1520-0469(1984)041<3396:WITS>2.0.CO;2)
- Ehard, B., Kaifler, B., Kaifler, N., & Rapp, M. (2015). Evaluation of methods for gravity wave extraction from middle-atmospheric lidar temperature measurements. *Atmospheric Measurement Techniques*, 8(11), 4645–4655. <https://doi.org/10.5194/amt-8-4645-2015>
- Ehard, B., Kaifler, B., Dörnbrack, A., Preusse, P., Eckermann, S. D., Bramberger, M., ... Rapp, M. (2017). Horizontal propagation of large-amplitude mountain waves into the polar night jet. *Journal of Geophysical Research: Atmospheres*, 122, 1423–1436. <https://doi.org/10.1002/2016JD025621>
- Eliassen, A., & Palm, E. (1961). On the transfer of energy in stationary mountain waves. *Geofysiske Publikasjoner*, 22, 1–23.
- Fritts, D. C., & Alexander, M. J. (2003). Gravity wave dynamics and effects in the middle atmosphere. *Reviews of Geophysics*, 41, 1003. <https://doi.org/10.1029/2001RG000106>
- Fritts, D. C., & Dunkerton, T. J. (1985). Fluxes of heat and constituents due to convectively unstable gravity waves. *Journal of Atmospheric Sciences*, 42(6), 549–556. [https://doi.org/10.1175/1520-0469\(1985\)042<0549:FOHACD>2.0.CO;2](https://doi.org/10.1175/1520-0469(1985)042<0549:FOHACD>2.0.CO;2)
- Fritts, D. C., Smith, R. B., Taylor, M. J., Doyle, J. D., Eckermann, S. D., Dornbrack, A., ... Ma, J. (2016). The deep propagating gravity wave experiment (DEEPWAVE): An airborne and ground-based exploration of gravity wave propagation and effects from their sources throughout the lower and middle atmosphere. *Bulletin of the American Meteorological Society*, 97(3), 425–453. <https://doi.org/10.1175/BAMS-D-14-00269.1>
- Garcia, F. J., Taylor, M. J., & Kelley, M. C. (1997). Two-dimensional spectral analysis of mesospheric airglow image data. *Applied Optics*, 36(29), 7374–7385. <https://doi.org/10.1364/AO.36.007374>
- Geller, M. A., & Gong, J. (2010). Gravity wave kinetic, potential, and vertical fluctuation energies as indicators of different frequency gravity waves. *Journal of Geophysical Research*, 115, D11111. <https://doi.org/10.1029/2009JD012266>
- Geller, M. A., Alexander, M. J., Love, P. T., Bacmeister, J., Ern, M., Hertzog, A., ... Zhou, T. (2016). A comparison between gravity wave momentum fluxes in observations and climate models. *Journal of Climate*, 26(17), 6383–6405. <https://doi.org/10.1175/JCLI-D-12-00545.1>
- Giez, A., Mallaun, C., Zöger, M., Dörnbrack, A., & Schumann, U. (2017). Static pressure from aircraft trailing-cone measurements and numerical weather-prediction analysis. *Journal of Aircraft*, 54(5), 1728–1737. <https://doi.org/10.2514/1.C034084>
- Gill, A. E. (1982). Atmosphere-ocean dynamics (pp. 662).
- Gisinger, S., Dörnbrack, A., Matthias, V., Doyle, J. D., Eckermann, S. D., Ehard, B., ... Rapp, M. (2017). Atmospheric Conditions during the Deep Propagating Gravity Wave Experiment (DEEPWAVE). *Monthly Weather Review*, 145, 4249–4275. <https://doi.org/10.1175/MWR-D-16-0435.1>
- Heale, C. J., Bossert, K., Snively, J. B., Fritts, D. C., Pautet, P.-D., & Taylor, M. J. (2017). Numerical modeling of a multiscale gravity wave event and its airglow signatures over Mount Cook, New Zealand, during the DEEPWAVE campaign. *Journal of Geophysical Research: Atmospheres*, 122, 846–860. <https://doi.org/10.1002/2016JD025700>
- Hildebrand, J., Baumgarten, G., Fiedler, J., & Lübken, F.-J. (2017). Winds and temperatures of the Arctic middle atmosphere during January measured by Doppler lidar. *Atmospheric Chemistry and Physics Discussions*, 2017, 1–23. <https://doi.org/10.5194/acp-2017-167>
- Hoffmann, L., Grimsdell, A. W., & Alexander, M. J. (2016). Stratospheric gravity waves at Southern Hemisphere orographic hotspots: 2003–2014 AIRS/Aqua observations. *Atmospheric Chemistry and Physics*, 16(14), 9381–9397. <https://doi.org/10.5194/acp-16-9381-2016>
- Holton, J., Curry, J., & Pyle, J. (2003). *Encyclopedia of atmospheric sciences*, no. Bd. 4 in Encyclopedia of Atmospheric Sciences: Academic Press.
- Holton, J. R. (1982). The role of gravity wave induced drag and diffusion in the momentum budget of the mesosphere. *Journal of Atmospheric Sciences*, 39(4), 791–799. [https://doi.org/10.1175/1520-0469\(1982\)039<0791:TROGWI>2.0.CO;2](https://doi.org/10.1175/1520-0469(1982)039<0791:TROGWI>2.0.CO;2)
- Kaifler, B., Lübken, F.-J., Höfner, J., Morris, R. J., & Viehl, T. P. (2015). Lidar observations of gravity wave activity in the middle atmosphere over Davis (69° S, 78° E), Antarctica. *Journal of Geophysical Research: Atmospheres*, 120, 4506–4521. <https://doi.org/10.1002/2014JD022879>
- Kaifler, B., Kaifler, N., Ehard, B., Dörnbrack, A., Rapp, M., & Fritts, D. C. (2015). Influences of source conditions on mountain wave penetration into the stratosphere and mesosphere. *Geophysical Research Letters*, 42, 9488–9494. <https://doi.org/10.1002/2015GL066465>

- Kaifler, N., Kaifler, B., Ehard, B., Gisinger, S., Dornbrack, A., Rapp, M., ... Liley, B. (2017). Observational indications of downward-propagating gravity waves in middle atmosphere lidar data. *Journal of Atmospheric and Solar-Terrestrial Physics*, 162, 16–27. <https://doi.org/10.1016/j.jastp.2017.03.003>
- Kirshbaum, D. J. (2017). On upstream blocking over heated mountain ridges. *Quarterly Journal of the Royal Meteorological Society*, 143(702), 53–68. <https://doi.org/10.1002/qj.2945>
- Kruse, C. G., & Smith, R. B. (2015). Gravity wave diagnostics and characteristics in mesoscale fields. *Journal of Atmospheric Sciences*, 72(11), 4372–4392. <https://doi.org/10.1175/JAS-D-15-0079.1>
- Kruse, C. G., Smith, R. B., & Eckermann, S. D. (2016). The midlatitude lower-stratospheric mountain wave "valve layer". *Journal of Atmospheric Sciences*, 73(12), 5081–5100. <https://doi.org/10.1175/JAS-D-16-0173.1>
- Le Pichon, A., Assink, J., Heinrich, P., Blanc, E., Charlton-Perez, A., Lee, C., ... Claud, C. (2015). Comparison of co-located independent ground-based middle atmospheric wind and temperature measurements with numerical weather prediction models. *Journal of Geophysical Research: Atmospheres*, 120(16), 8318–8331. <https://doi.org/10.1002/2015JD023273>
- Lilly, D. K., & Kennedy, P. J. (1973). Observations of a stationary mountain wave and its associated momentum flux and energy dissipation. *Journal of Atmospheric Sciences*, 30(6), 1135–1152. [https://doi.org/10.1175/1520-0469\(1973\)030<1135:OASMW>2.0.CO;2](https://doi.org/10.1175/1520-0469(1973)030<1135:OASMW>2.0.CO;2)
- Lu, X., Chen, C., Huang, W., Smith, J. A., Chu, X., Yuan, T., ... Cullens, C. Y. (2015). A coordinated study of 1h mesoscale gravity waves propagating from Logan to Boulder with CRRL Na Doppler lidars and temperature mapper. *Journal of Geophysical Research: Atmospheres*, 120, 10,006–10,021. <https://doi.org/10.1002/2015JD023604>
- Mallaun, C., Giez, A., & Baumann, R. (2015). Calibration of 3-D wind measurements on a single-engine research aircraft. *Atmospheric Measurement Techniques*, 8, 3177–3196. <https://doi.org/10.5194/amt-8-3177-2015>
- Meischner, P., Baumann, R., Höller, H., & Jank, T. (2001). Eddy dissipation rates in thunderstorms estimated by doppler radar in relation to aircraft in situ measurements. *Journal of Atmospheric and Oceanic Technology*, 18, 1609–1627. [https://doi.org/10.1175/1520-0426\(2001\)018<1609:EDRITE>2.0.CO;2](https://doi.org/10.1175/1520-0426(2001)018<1609:EDRITE>2.0.CO;2)
- Nappo, C. J. (2013). *An introduction to atmospheric gravity waves*, International Geophysics Series (2nd edn., Vol. 85, p. 276). Waltham, MA: Academic Press.
- Ólafsson, H., & Bougeault, P. (1996). Nonlinear flow past an elliptic mountain ridge. *Journal of Atmospheric Sciences*, 53(17), 2465–2489. [https://doi.org/10.1175/1520-0469\(1996\)053<2465:NFAEM>2.0.CO;2](https://doi.org/10.1175/1520-0469(1996)053<2465:NFAEM>2.0.CO;2)
- Pautet, P.-D., Taylor, M. J., Pendleton, W. R., Zhao, Y., Yuan, T., Esplin, R., & McLain, D. (2014). Advanced mesospheric temperature mapper for high-latitude airglow studies. *Applied Optics*, 53(26), 5934–5943. <https://doi.org/10.1364/AO.53.005934>
- Pautet, P.-D., Taylor, M. J., Fritts, D. C., Bossert, K., Williams, B. P., Broutman, D., ... Doyle, J. D. (2016). Large-amplitude mesospheric response to an orographic wave generated over the Southern Ocean Auckland Islands (50.7°S) during the DEEPWAVE project. *Journal of Geophysical Research: Atmospheres*, 121, 1431–1441. <https://doi.org/10.1002/2015JD024336>
- Pierrehumbert, R. T., & Wyman, B. (1985). Upstream effects of mesoscale mountains. *Journal of Atmospheric Sciences*, 42(10), 977–1003. [https://doi.org/10.1175/1520-0469\(1985\)042<0977:UEOMM>2.0.CO;2](https://doi.org/10.1175/1520-0469(1985)042<0977:UEOMM>2.0.CO;2)
- Plougonven, R., & Zhang, F. (2014). Internal gravity waves from atmospheric jets and fronts. *Reviews of Geophysics*, 52, 33–76. <https://doi.org/10.1002/2012RG000419>
- Rapp, M., Strelnikov, B., Müllemann, A., Lübken, F.-J., & Fritts, D. C. (2004). Turbulence measurements and implications for gravity wave dissipation during the MacWAVE/MIDAS rocket program. *Geophysical Research Letters*, 31(24), L24S07. <https://doi.org/10.1029/2003GL019325>
- Reinecke, P. A., & Durran, D. R. (2008). Estimating topographic blocking using a Froude number when the static stability is nonuniform. *Journal of Atmospheric Sciences*, 65(3), 1035–1048. <https://doi.org/10.1175/2007JAS2100.1>
- Sato, K. (1990). Vertical wind disturbances in the troposphere and lower stratosphere observed by the MU radar. *Journal of Atmospheric Sciences*, 47(23), 2803–2817. [https://doi.org/10.1175/1520-0469\(1990\)047<2803:VWDITT>2.0.CO;2](https://doi.org/10.1175/1520-0469(1990)047<2803:VWDITT>2.0.CO;2)
- Sato, K., & Dunkerton, T. J. (1997). Estimates of momentum flux associated with equatorial Kelvin and gravity waves. *Journal of Geophysical Research*, 102(D22), 26,247–26,261. <https://doi.org/10.1029/96JD02514>
- Sato, K., Tateno, S., Watanabe, S., & Kawatani, Y. (2012). Gravity wave characteristics in the southern hemisphere revealed by a high-resolution middle-atmosphere general circulation model. *Journal of Atmospheric Sciences*, 69(4), 1378–1396. <https://doi.org/10.1175/JAS-D-11-0101.1>
- Sato, K., Watanabe, S., Kawatani, Y., Tomikawa, Y., Miyazaki, K., & Takahashi, M. (2009). On the origins of mesospheric gravity waves. *Geophysical Research Letters*, 36, L19801. <https://doi.org/10.1029/2009GL039908>
- Satomura, T., & Sato, K. (1999). Secondary generation of gravity waves associated with the breaking of mountain waves. *Journal of Atmospheric Sciences*, 56(22), 3847–3858. [https://doi.org/10.1175/1520-0469\(1999\)056<3847:SGOGWA>2.0.CO;2](https://doi.org/10.1175/1520-0469(1999)056<3847:SGOGWA>2.0.CO;2)
- Smith, R. B., & Kruse, C. G. (2017). Broad-spectrum mountain waves. *Journal of Atmospheric Sciences*, 74(5), 1381–1402. <https://doi.org/10.1175/JAS-D-16-0297.1>
- Smith, S., Baumgardner, J., & Mendillo, M. (2009). Evidence of mesospheric gravity-waves generated by orographic forcing in the troposphere. *Geophysical Research Letters*, 36, L08807. <https://doi.org/10.1029/2008GL036936>
- Smith, R. B., Woods, B. K., Jensen, J., Cooper, W. A., Doyle, J. D., Jiang, Q., & Grubišić, V. (2008). Mountain waves entering the stratosphere. *Journal of Atmospheric Sciences*, 65(8), 2543–2562. <https://doi.org/10.1175/2007JAS2598.1>
- Smith, R. B., Nugent, A. D., Kruse, C. G., Fritts, D. C., Doyle, J. D., Eckermann, S. D., ... Beaton, S. (2016). Stratospheric gravity wave fluxes and scales during DEEPWAVE. *Journal of Atmospheric Sciences*, 73(7), 2851–2869. <https://doi.org/10.1175/JAS-D-15-0324.1>
- Taylor, M. J., Pautet, P.-D., Medeiros, A. F., Buriti, R., Fecine, J., Fritts, D. C., ... São Sabbas, F. T. (2009). Characteristics of mesospheric gravity waves near the magnetic equator, Brazil, during the SpreadFex campaign. *Annals of Geophysics*, 27(2), 461–472. <https://doi.org/10.5194/angeo-27-461-2009>
- Teixeira, M. (2014). The physics of orographic gravity wave drag. *Frontiers in Physics*, 2, 1–24.
- Torrence, C., & Compo, G. P. (1998). A practical guide to wavelet analysis. *Bulletin of the American Meteorological Society*, 79(1), 61–78. [https://doi.org/10.1175/1520-0477\(1998\)079<0061:APGTWA>2.0.CO;2](https://doi.org/10.1175/1520-0477(1998)079<0061:APGTWA>2.0.CO;2)
- Vadas, S. L., Fritts, D. C., & Alexander, M. J. (2003). Mechanism for the generation of secondary waves in wave breaking regions. *Journal of Atmospheric Sciences*, 60(1), 194–214. [https://doi.org/10.1175/1520-0469\(2003\)060<0194:MFTGOS>2.0.CO;2](https://doi.org/10.1175/1520-0469(2003)060<0194:MFTGOS>2.0.CO;2)
- Vadas, S. L., Taylor, M. J., Pautet, P.-D., Stamus, P. A., Fritts, D. C., Liu, H.-L., ... Takahashi, H. (2009). Convection: the likely source of the medium-scale gravity waves observed in the OH airglow layer near Brasília, Brazil, during the SpreadFex campaign. *Annales Geophysicae*, 27(1), 231–259. <https://doi.org/10.5194/angeo-27-231-2009>
- Vosper, S. B. (2015). Mountain waves and wakes generated by South Georgia: Implications for drag parametrization. *Quarterly Journal of the Royal Meteorological Society*, 141(692), 2813–2827. <https://doi.org/10.1002/qj.2566>

- Vosper, S. B., Brown, A. R., & Webster, S. (2016). Orographic drag on islands in the NWP mountain grey zone. *Quarterly Journal of the Royal Meteorological Society*, 142(701), 3128–3137. <https://doi.org/10.1002/qj.2894>
- Wagner, J., Dörnbrack, A., Rapp, M., Gisinger, S., Ehard, B., Bramberger, M., ... Hoor, P. (2017). Observed versus simulated mountain waves over Scandinavia—Improvement of vertical winds, energy and momentum fluxes by enhanced model resolution? *Atmospheric Chemistry and Physics*, 17(6), 4031–4052. <https://doi.org/10.5194/acp-17-4031-2017>
- Witschas, B., Rahm, S., Dörnbrack, A., Wagner, J., & Rapp, M. (2017). Airborne wind lidar measurements of vertical and horizontal winds for the investigation of orographically induced gravity waves. *Journal of Atmospheric and Oceanic Technology*, 34(6), 1371–1386. <https://doi.org/10.1175/JTECH-D-17-0021.1>
- Woods, B. K., & Smith, R. B. (2010). Energy flux and wavelet diagnostics of secondary mountain waves. *Journal of Atmospheric Sciences*, 67(11), 3721–3738. <https://doi.org/10.1175/2009JAS3285.1>
- Wrasse, C. M., Nakamura, T., Takahashi, H., Medeiros, A. F., Taylor, M. J., Gobbi, D., ... Admiranto, A. G. (2006). Mesospheric gravity waves observed near equatorial and low-middle latitude stations: Wave characteristics and reverse ray tracing results. *Annals of Geophysics*, 24(12), 3229–3240. <https://doi.org/10.5194/angeo-24-3229-2006>